This is to certify that the
thesis entitled

EXPERIMENTAL INVESTIGATION OF FLOW IN A
RECTANGULAR CAVITY WITH A POROUS OPENING

presented by

SAGAR RAYEPALLI

has been accepted towards fulfillment
of the requirements for the

M.S. degree in Mechanical Engineering

M. M. Kaviani
Major Professor's Signature

11/07/2007
Date

EXPERIMENTAL INVESTIGATION OF FLOW IN A RECTANGULAR CAVITY WITH A POROUS OPENING

By

Sagar Rayepalli

A THESIS

Submitted to
Michigan State University
in partial fulfillment of the requirements
for the degree of

MASTER OF SCIENCE

Department of Mechanical Engineering

2007

ABSTRACT

EXPERIMENTAL INVESTIGATION OF FLOW IN A RECTANGULAR CAVITY WITH A POROUS OPENING

By

Sagar Rayepalli

The velocity field within a nominally two-dimensional cavity is investigated in a water channel. The Reynolds number based on cavity length and freestream speed is in the range 245 – 410. The purpose of the study is to characterize the changes in the recirculation flow pattern inside the cavity caused by a porous surface (rectangular mesh) covering the cavity opening. Both flow visualization and quantitative results for the mean and fluctuating velocity field are discussed for surfaces of different porosity ranging between 64.8% and 37.3%. The total kinetic energy, vorticity distribution and related circulation in the cavity are analyzed. The most significant finding is the huge reduction in total kinetic energy when the cavity opening was covered with the mesh for all cases. It is observed that parameters such as positioning of mesh with respect to cavity, length of mesh exposed to flow, gap between the cavity and mesh also affect the flow field inside the cavity. And finally suggestions are made to minimize the flow field inside the cavity.

ACKNOWLEDGEMENTS

I take this opportunity to express my deep sense of gratitude and profound thanks to Dr. Manoochehr Koochesfahani, for the constant help, continual encouragement and guidance given to me during the course of my Masters' research. He has been a source of inspiration throughout the course of this work. But for his continuous guidance and help, I would not have completed this work successfully. I would also like to thank Dr. Brereton and Dr. Rishi Gupta for reviewing my manuscript.

I am indebted to my current and past lab mates: Dr. Chee Lum, Dr. Douglas Bohl, Shahram and Rajat Basu who provided me with valuable information regarding my work.

I dedicate this thesis to my family who unremittingly supported me and provided me constant encouragement during my years of study. They made this work possible.

Finally, I wish to place on record my deep sense of gratitude to Dr. Manoochehr Koochesfahani for all the help, guidance and encouragement extended by him for the successful completion of this work and cherish to remember my association with him.

Sagar Rayepalli

TABLE OF CONTENTS

LIST OF TABLES

LIST OF FIGURES

Images in this thesis/dissertation are presented in color.

LIST OF SYMBOLS

Symbol	*Description (page or figure of first reference)*
d	Diameter of mesh wire (10)
D	Diameter of silver coated hollow spheres (12)
DPIV	Digital particle image velocimetry (11)
g	Gravitational acceleration (12)
l	Rectangle size (10)
Re	Reynolds number based on cavity opening width (9)
TKE	Total kinetic energy (30)
$\overline{u}$	Mean component of X – velocity (22)
u'	Fluctuating component of X – velocity (22)
υ_T	Settling speed of particles (12)
$\overline{v}$	Mean component of Y – velocity (22)
v'	Fluctuating component of Y – velocity (22)
U_o	Freestream velocity (17)
y	Distance from the flat plate bottom surface (17)
δ	Boundary layer thickness (17)
η	$\frac{5y}{\delta}$ (17)
ρ_p	Density of silver coated hollow spheres (12)
ρ_f	Density of water (12)
υ	Kinematic viscosity (12)

1. INTRODUCTION

Research has been done on several aspects of cavity flows both experimentally and numerically. However, it is noted less or no research has been done on characterizing the changes in the recirculation flow pattern inside the cavity, caused by a porous surface covering the cavity opening. The primary motivation for this investigation was flow field analysis inside a brain aneurysm; minimization of flow fields within the aneurysm using a stent being one the aspects. Keeping this objective in mind, a fundamental study of flow field inside a 2D rectangular cavity with a porous opening would be useful before starting with analysis inside the aneurysm.

1.1 Cavity Flows

The study of cavity flows at low Reynolds numbers dates back several decades. Two types of cavity flows have been studied, both experimentally and numerically. They are:

1. Lid driven cavities

The problem geometry is simple and two-dimensional, and the boundary conditions are also simple. The standard case is fluid contained in a square domain with Dirichlet boundary conditions on all sides, with three stationary sides and one moving side (with velocity tangent to the side).

2. Shear driven cavities

For these types of flows, the lid is replaced with a moving fluid. The two names (lid-driven and shear-driven) are used interchangeably in spite of the fact that they are distinct (and different) problems.

The problems of the cavity flows have been studied by several investigators. The streamlines have been analyzed theoretically by Moffatt (1963) and Takematsu (1966). Moffatt (1963) studied some simple similarity solutions for the flow of a viscous fluid near a sharp corner between two planes on which a variety of boundary conditions may be imposed. Takematsu (1966) studied the steady flow of a viscous incompressible fluid past a two-dimensional cavity of infinite depth. His analysis is based on Stokes approximation, i.e. the assumption that $Re <<< 1$ and the convection of vorticity is to be neglected. In his analysis he assumed the oncoming stream to be a parallel flow with constant vorticity, its speed being $U(y) = y$. He found that the dividing streamline was not consistent with the mouth of the cavity, although rather straight, but that it penetrates to a considerable depth into the cavity. He mentions that as far as the Stokes approximation was concerned, the separation of the flow occurs, not at the corner, but on the cavity wall.

Kawaguti (1961) has studied the two-dimensional rectangular cavity flows (lid driven type) to obtain the distributions of stream function, vorticity and pressure. He computed the results for low Reynolds numbers ranging from 0 (Stokes' solution) to 64 and for various cavity lengths. He concluded that in all cases, the pressure on the downstream edge of the cavity is higher and that on the upstream was lower compared to middle point of the bottom wall. He also found that as Reynolds number was increased, the centre of

the vortex moves downstream, and the pressure gradient in the region downstream becomes steeper, while that in the region upstream less steep.

Kinoshita, O. and Ito, H. (1984) have experimentally studied the two-dimensional flow of an oblique cavity (lid driven type) for a very low Reynolds numbers (Re << 1) using tracer techniques. They compared their results with numerical simulations of Kawaguti (1961) and found solutions to be nearly consistent.

Manovski, P. (2005) experimentally investigated two-dimensional rectangular cavity for several cavity lengths, for Reynolds numbers 90 – 730. Planar laser induced fluorescence (PLIF) was employed as a flow visualization method and particle image velocimetry (PIV) provided quantitative measurements of the complex velocity fields. His analysis was mainly related to an interesting aspect of cavity flow that is the initiation of self-sustained oscillations of the cavity shear layer between the freestream flow and the cavity fluid.

1.2 Brain Aneurysm

The details about the brain aneurysm and the current available treatment options are obtained from the website www.brainaneurysm.com. An aneurysm is an abnormal widening or ballooning of a portion of a blood vessel. A cerebral aneurysm refers to a blood vessel within the brain that weakens over time and undergoes such widening. This usually occurs at the junctions of the large arteries at the base of the brain, in an area called the Circle of Willis. As the blood vessel weakens, it begins to bulge out like a

balloon. Often, as an aneurysm develops, it forms a neck with an associated dome, or balloon like structure. As the artorial wall weakens, the aneurysm may rupture.

Brain aneurysms are often discovered when they rupture, causing bleeding into the brain or the space closely surrounding the brain called the subarachnoid space, causing a subarachnoid hemorrhage. Subarachnoid hemorrhage from a ruptured brain aneurysm often leads to significant disability or death. It is estimated that up to one in 15 people in the United States will develop a brain aneurysm during their lifetime 6-8 / 100,000 patients will present with subarachnoid hemorrhage.

Surgery or minimally-invasive endovascular coiling techniques can be used in the treatment of brain aneurysms. Until recently, people with wide-necked aneurysms in the brain would not have been candidates for coil embolization, a procedure in which tiny coils are used to close off the aneurysm.

Historically, if the fundus to neck ratio was less than 2 then the coil embolization could not be performed satisfactorily due to coil loop herniation. The recent introduction of flexible intracranial stents has provided a method of preventing the coil from migrating out of wide-necked aneurysms. The stent is placed across the neck of the aneurysm prior to introduction of coils into the aneurysm. Therefore, more patients can undergo minimally invasive interventions to repair their cerebral aneurysms. The body responds by forming a blood clot thrombosis around the coils and new tissue growth around the stent to prevent blood flow into the aneurysm cavity. Coiling introduces the risk of perforation of the aneurysm when the coils are introduced. There is also a risk of

thrombus formation that can dislodge into the parent vessel and also of coil protrusion into the parent vessel.

Recently, intravascular porous tubular-shaped stents are being considered for the endovascular treatment of intracranial aneurysms. Flow field analysis inside a brain aneurysm in the presence of stent is one of the interesting areas. Research in this area is being done for the past decade by several researchers. They have studied the effect of stent porosity and influence of aneurysm geometry on the flow inside the aneurysm.

Lieber, B.B., Stancampiano, A.P. and Wakhlooo, A.K. (1997), investigated the changes in local hemodynamics resulting from stent implantation. They used woven nitinol stents of porosities 76%, 80%, 82% and 85%. Womersley number was 5.3 for large arteries and 2.7 for small arteries. The mean, maximum, minimum Reynolds number for large arteries was 180, 490, and 30 respectively and 90, 230 and 2 respectively for small arteries. They found that for both large and small arteries placement of a stent of lowest porosity across the aneurysm orifice resulted in substantial reduction of aneurysmal vortex speed and decreased interaction with parent vessel. Their results are based on flow visualization (qualitative analysis) using laser-induced fluorescence of Rhodamine dye. Measurements related to kinetic energy reduction due to the presence of stent were not studied.

Yu, S.C.M., Zhao, J.B. (1999) have done steady flow analysis on the stented and non stented sidewall aneurysm models using particle image velocimetry techniques. They found that the highest wall shear stresses (derived from near wall velocity measurements) always appear at the distal neck of the aneurysmal pouch. Their investigations are limited to only steady state flow analysis and haven't made any measurements for pulsatile

flows. Rhee, K., Han, M.H. and Cha S.H. (2002) studied the changes of flow characteristics by stenting in aneurysm models for a pulsatile flow. In addition to influence of stent porosity, they also studied the effect of aneurysm geometry. In their study they clarified the velocity and wall shear stress changes that are caused by stenting in fusiform and lateral aneurysm models. Even, their results are also completely based on flow visualization of photochromic dye that was 1', 3', 3'-trimethyl-6-nitroindoline-6-spiro-benzospyran (TNSB). Their analysis is purely qualitative in nature and they haven't commented on total kinetic energy reduction caused by the placement of stent.

Chee Lum (2007) has made quantitative measurements inside a glass model (Figure 1) of brain aneurysm. The stent used in that experiment has a diameter of 5 mm and the wire thickness of it is 0.1077 mm. The aneurysm opening was 6.5 mm wide and the percentage opening area of the stent was 80%. This experiment was done at Reynolds number of 184 (based on tube diameter) and 267 (based on aneurysm opening diameter). The measured velocity field inside the aneurysm with/without the stent is shown in Figure 2. He reported that the average total kinetic energy decreased to 9.6% (Figure 3) when the aneurysm opening was covered with the stent. He observed that the vortex core lies towards the downstream edge of the aneurysm cavity (Figure 4).

The flow characteristics inside the aneurysm pouch could be significantly affected by the selection of stent, the shape of aneurysm and the type of flow. To the best knowledge of author very little research has been done to estimate reduction (from quantitative measurements) in total kinetic energy for pulsatile flows. Therefore, a detailed study of velocity field, total kinetic energy distribution, vorticity distribution, wall shear stress

changes inside the aneurysm pouch for a pulsatile flow caused by stenting, is felt to be of importance. The results from these experiments would comprehend the results from little known research.

At present in the Turbulent Mixing and Unsteady Aerodynamics Laboratory (Michigan State University, East Lansing), stents of different porosity are not available to carry out the experimental analysis on the glass model of brain aneurysm. So, as a starting point, a fundamental study of flow field inside a 2D rectangular cavity with a porous opening it is felt to be of use. Furthermore, it is limited to steady state analysis. The results from 2D rectangular cavity experiment are compared with the aneurysm result of Chee Lum (2007), to check whether the porous surface near the cavity opening has similar effect on aneurysm and 2D rectangular cavity.

2. EXPERIMENTAL FACILITY AND INSTRUMENTATION

All of the experiments used for this study were performed in the Turbulent Mixing and Unsteady Aerodynamics Laboratory's (Michigan State University, East Lansing) small water tunnel facility. The present study is based on the results from streamwise imaging. This chapter will explain the experimental facility and diagnostics. Images in this thesis/dissertation are presented in color.

2.1 Experimental Facility

All of the experiments were performed in a water tunnel, which was driven by Baldor electric motor attached with a Fincor 5200 adjustable frequency ac motor control as illustrated in Figure 5. The test section used in this study had inside dimensions of 19 cm (height) x 15.3 cm (width) x 43.4 cm (length). During the experiment the water tunnel was filled with deionized water with a hose up to a height of 14.2 cm from the test section base. Extreme care was taken in filling the test section to reduce bubbles that could upset the flow characteristics of the approach stream. Uniform, laminar flow was ensured in the test section by using a series of honeycombs and fine screens upstream of the contraction.

A flat two – dimensional flat plate of 1.7 cm thickness was placed in the water tunnel at a distance of 8.5 cm (measured from the bottom face of flat plate to the bottom of the test section) with the help support rods as shown in Figure 6(a). The rounded leading edge of the flat plate is half circular while the trailing edge is tapered. An arrangement was

provided within the flat plate to place a two – dimensional rectangular cavity of different sizes. The length of the cavity used in the experiment is 0.5 cm and depth of is 0.52 cm. The front edge of the cavity is located at a distance of 17.3 cm from the leading edge of the flat plate.

The experiments were done at three different motor frequencies namely 6 Hz, 8 Hz and 10 Hz. The motor has the capability to reach a maximum of 60 Hz. The Reynolds number (Re) of the freestream (with flat plate in the test section) was measured based on the cavity length of 0.5 cm. The experiments were done over a period of several months and so the knob (used to adjust the water tunnel motor frequency) position may not exactly coincide with the previous knob positions. So, for a particular motor frequency the free stream velocity is not a constant value but, varies within a certain range. The range of Reynolds numbers for 6 Hz, 8 Hz, and 10 Hz frequencies are listed in Table 1. Table 13 in Appendix A shows the water tunnel calibration data up to a motor frequency of 18 Hz and is plotted in Figure 7.

Table 1. Reynolds number range for 6,8,10 Hz frequencies of water tunnel motor

Water Tunnel Motor Frequency (Hz)	Reynolds Number (based on cavity length = 0.5 cm)
6	245 - 265
8	310 - 340
10	370 - 410

Seven different sizes of stainless steel woven mesh are used in the cavity flow experiments. Their specifications namely, wire diameter, percentage opening area, rectangle size and cell per inch are listed in Table 2. The diameters of the wire meshes are

chosen in such a way that they are roughly about the same wire diameter as that of the stent (0.1077 mm) used by Chee Lum (2007) in his experiments. Rectangle size is defined as the distance between adjacent wires in the wire mesh as shown in Figure 8. The percentage opening area of mesh is given by equation 2.1.

$$Percentage\ opening\ area = \frac{l^2}{(l+d)^2} \times 100 \tag{2.1}$$

Table 2. Mesh specifications

Wire diameter (mm)	Percentage open area	Rectangle size (mm)	Cell per inch
0.1397	49.4	0.3302	54 x 54
0.1397	59.1	0.4572	42 x 42
0.1651	37.3	0.2540	60 x 60
0.1651	56.7	0.5080	38 x 38
0.1651	64.8	0.6807	30 x 30
0.1905	39.1	0.3302	50 x 50
0.1905	64.8	0.7874	26 x 26

Five different sets of experiments involving the mesh were conducted namely, study of effect of percentage opening area of mesh (Figure 9(a)), study of effect of rectangle size (Figure 9(a)), study of effect of positioning of mesh with respect to the cavity, study of effect of exposed length of mesh (Figure 9(b)) and study of effect of gap between the mesh and cavity (Figure 10).

For all experiments, expect the experiments involving the study of the effect of length of mesh, the length of the mesh used was 2 cm. The mesh was attached to the flat plate symmetrical to the cavity using a black vinyl electrical tape of 0.215 mm thickness as

shown in Figure 9(a). Except the cavity opening length of 0.5 cm, the mesh was covered with a tape of length 0.75 cm upstream and downstream to the cavity edges. Three experiments involving a gap between the cavity and mesh were performed and the gap was maintained using shim stocks of thickness 0.127 mm, 0.254 mm and 0.508 mm.

2.2 Diagnostics

Digital Particle Image Velocimetry (DPIV) technique was used to measure two components of velocity in a plane parallel to the streamwise direction and perpendicular to spanwise direction. The DPIV apparatus consisted of a light source (laser), camera and a PC equipped with a frame grabber. The laser acts as a photographic flash for the camera, and the particles in the fluid scatter the light. It was this scattered light that was detected by the camera.

In order to measure the velocity at least two exposures are needed. They are recorded on two separate frames. The frames were split in a large number of interrogation areas, often called tiles/windows. It was then possible to calculate a displacement vector for each tile with help of cross-correlation program. This was converted to a velocity using the time between image exposures. Spacing between image exposures was controlled by timing electronics. The electronics also permitted image pairs to be acquired at various times along the flow. These digital delay and pulse generators provided several outputs that can be delayed and referenced to each other.

The fluid under investigation (deionized water) was first seeded with tracer articles that followed flow field. It is the motion of these seeding particles that is used to calculate velocity information. The seed particles used in the experiment are CONDUCT-O-FIL® silver-coated hollow glass spheres (Potter Industries Inc. - SH400S20). The properties of the particles are mentioned in Table 3.

Table 3. Properties of silver-coated hollow glass spheres

% Ag metal	20
D10 (μm)	6
D90 (μm)	33
True Density (g/cc)	1.6

In Table 3 D10 implies 10 percent of particles are smaller than 6 μm and similarly D90 implies 90 percent of particles are smaller than 33 μm. Eames (2004) in his paper showed the settling speed of a particle, v_T to be equation 2.2. In equation 2.2, assuming diameter of the particle to be D50 i.e. 19.5 μm, the settling speed of the particles in water was measured to be 0.124 mm/s. The settling speed could affect the results of flow field inside the cavity, when dealing with either low Reynolds numbers or low percentage opening areas of mesh. The effect of the settling speed will be discussed in detail in the later chapters while dealing with quantitative results of flow field inside the cavity.

$$v_T = \frac{g\left(\rho_p / \rho_f - 1\right)D^2}{18\upsilon} \qquad (2.2)$$

A 500 mW Lasiris Magnum SP Laser operating at a wavelength of 680nm was used as the light source. It was mounted on top of the test section with the help of 80/20® Inc.'s aluminum T-slotted profiles (20 series). Laser line patterns are often generated by

cylindrical optics that produce a Gaussian line profile with a bright centre and fading ends. Lasiris optics spread the laser beam into an evenly illuminated line along the streamwise direction. The laser is focusable and was adjusted to produce a focus line at desired distance. In addition the line was collimated so that its thickness (approximately 200 μm thickness) remains fairly constant over a long projection distance.

The imaging was done using two different cameras. Pixelfly camera was used to make flow measurements inside the cavity because of its higher resolution and Pulnix TM-9701 CCD camera was used to make freestream speed measurements.

The streamwise imaging arrangement for Pixelfly camera is shown in Fig 11. A Pixelfly camera with a resolution of 1392 (horizontal) x 1024 (vertical) pixels (focus area - 0.928 cm x 0.683 cm) was used to image the cavity in the setup. It was operated with an exposure of 400 ms (2.5 frames/s) for particle streak flow visualization within the cavity and laser was shot continuously. Since the exposure was maintained same for all cases during the experiment, one can figure out the difference in velocities qualitatively based on streak lengths. Using a Pixelfly camera the maximum frame rate that can be achieved was 11.5 fps. So, for velocity measurements the camera exposure was maintained at 100 ms (10 fps) but, the actual exposure was given by laser pulse width. It was operated in video mode. Table 10-12 shows the pulse widths used for different sets of experiments. Micro-Nikkor 105 mm f/2.8 lens was mounted on the camera. Nikon Teleconverter (TC – 201), Quantaray Double Ranger 7 EL were also mounted between the lens and the Pixelfly camera, to multiply the primary lens's focal length by a factor of 2X each. While

on the other hand, they decrease the effective aperture of the primary lens by two f-stops each.

Camware was the control software for Pixelfly camera. It's a 32-bit application for the Windows 9x/ME/2000/NT operating systems. The image acquired using Camware was stored as 16 bit TIFF image (2.72 MB each). It was converted to 8-bit TIFF image (1.36 MB) using Image-Pro Plus 5.0 software. 125 image pairs are acquired for quantitative analysis i.e. 125 velocity field samples.

Schematic of timing diagram for Pixelfly camera is illustrated in Figure 12-13. In case of cavity flow measurements, the timing and duration of light pulses was attained with the help of 3 SRS 4-Channel digital delay/pulse generators (Model DG535) and one 2 – channel AND gate. The first delay generator was used to generate an internal 10 Hz signal which was provided to both camera and second delay generator. In video mode setting of Pixelfly camera there is an intrinsic + system delay of 130 μs. So, the first delay generator is operated at 9.987 Hz (100130 μs) so that the resultant output would be 10 Hz (10^5 μs) signal. The second delay generator converts that 10 Hz signal to 5 Hz. The third produces two pulses of desired pulse width and delay, such that first pulse lies at the end of first camera frame and second pulse at the beginning of the next camera frame. The AND gate combines the 2 pulses and then transmits the combined signal to the laser. The separation time between light pulses depends on the velocity range and the size of the interrogation region. This is because accurate PIV velocity estimates require that the

majority of the particles located in the interrogation region in the first image remain within the corresponding region in the second image.

In this case the light source was pulsed with a pulse width in the range 2 – 50 ms for an incavity maximum speed of 3.80 - 0.19 cm/s respectively. And the delay periods between pulses vary in the range 15 – 900ms. For a delay period of more than 200 ms, a slightly different strategy was adopted. The flow was imaged at 10 fps with a delay period of 100ms and every second or third or fourth so on images were correlated depending on the flow speed. If every second image was correlated it implies the delay period was 200ms. Similarly, if the delay period was 300ms then, every third image was correlated. Table 10-12 in Appendix A gives the complete list of pulse widths and delay periods for various experiments.

Figure 14 illustrates the arrangement for freestream speed imaging using Pulnix TM-9701 CCD camera. Pulnix TM-9701 CCD camera with a resolution of 640 (horizontal) x 480 (vertical) pixels (focus area - 5.07 cm x 3.8 cm) was used for this. Standard video framing rate (30 frames/s or 60 fields/s) was digitized to 8 bits (300 KB) and recorded onto hard disk (as TIFF image) in real time by an image acquisition system (Mutech MV1000 Capture Sequence). 30 image pairs were recorded for freestream velocity calculations using digital particle image velocimetry.

Schematic of timing diagram for the Pulnix TM-9701 CCD camera is illustrated in Figure 15-16. In the case of freestream measurements, the timing and duration of light pulses

was attained with the help of Color Sync, 2 SRS 4-Channel digital delay/pulse generators (Model DG535) and a 2 – channel AND gate. The Color Sync was used to generate the 30 Hz (60 VD) reference signal. It was provided to both camera and first delay generator. The first delay generator converts that 30 Hz signal to 15 Hz. The second produces two pulses of desired pulse width and delay, which was combined by AND gate and then transmitted to laser. Table 13 in Appendix A gives the list of pulse widths and delay periods for freestream velocities measured.

The DPIV data were processed using the in-house MTV processing programs. The program was broken down into three categories: pre-processing, processing, post-processing. The preprocessing step readies the data and the inputs for the correlation step. The post-processing step allows the user to extract statistics and prepare the output for plotting. All images used in the MTV processing routines are TIFF images. The typical sequence of steps used for processing the DPIV data is listed in Appendix B.

3. RESULTS AND DISCUSSION

This chapter presents visual and quantitative results of the effect of several parameters namely, percentage opening area, rectangle size, length of mesh, positioning of mesh with respect to cavity and also effect of gap between mesh and cavity at three different water tunnel motor frequencies. The corresponding Reynolds number of those 3 frequencies is mentioned in Table 1. Details of the boundary layer thickness, upstream of the cavity are also discussed. Images in this thesis/dissertation are presented in color. In the analysis the direction of positive vorticity is considered to be into the plane, which is opposite to the standard convention i.e. out of the plane.

3.1 Boundary layer Thickness

The upstream edge of the cavity is located at a distance of 17.3 cm from the leading edge of the flat plate. The boundary layer starts developing at the leading edge and its thickness was measured at 2 locations upstream of the cavity, for three different Reynolds numbers. Using the measured boundary layer thickness (at 99% U_o), dimensionless measured velocity profiles were plotted and compared with Blasius solution (Equation 3.1).

$$f'(\eta) = \frac{u}{U_o}, \text{ where } \eta = \frac{5y}{\delta} \tag{3.1}$$

Case 1: Upstream Length = 1.8 cm (15.5 cm from the leading edge of flat plate)

Figure 17 (a) shows the velocity profiles measured at a length of 1.8 cm upstream to the upstream edge of the cavity. The measured velocity profiles are slightly off from the Blasius solution.

For a free stream velocity, U_o of 7.48 cm/s (Re = 374.15), 6.5 cm/s (Re = 325.1), 5.031 cm/s (Re = 251.56) the boundary layer thickness was measured to be 0.74 cm, 0.774 cm, 0.851 cm respectively.

Case 2: Upstream Length = 0.04 cm (17.26 cm from the leading edge of flat plate)

Figure 17(b) shows the velocity profiles measured at a length of 0.04 cm upstream to the upstream edge of the cavity. The measured velocity profiles at an upstream length of 0.04 cm deviates from the Blasius solution, more compared to the velocity profiles at an upstream length of 1.8 cm. The velocities are higher through out the measured velocity profiles compared to Blasius solution. In all the three measured velocity profiles, points very near to the wall (first 4 points) behave slightly different compared to remaining part of the profile. The reason for this behavior could be because of the presence of cavity, just 0.04 cm downstream of this measured point.

For a free stream velocity, U_o of 7.57 cm/s (Re = 378.49), 565 cm/s (Re = 328.26), 5.077 cm/s (Re = 253.87) the boundary layer thickness was measured to be 0.72 cm, 0.74 cm, 0.842 cm respectively.

3.2 Results of effect of percentage opening area of mesh

This part of the section presents the visual and quantitative results of the effect of percentage opening area. The results will be discussed only for Re $\approx$ 390, since the flow patterns are found to be similar at other Reynolds numbers too for most of the cases.

First for several cases, the particle streak flow visualizations will be presented which is followed by numerical results and finally the results will be discussed.

3.2.1. Flow Visualization

Figures 18-22 show the particle streak flow visualization of flow inside the 2-dimensional cavity. Flow visualizations are shown only for no mesh case and two mesh cases at all three Reynolds number. For other meshes the flow patterns are similar. Trajectories of particles are photographed in a long exposure. The exposure time was 400 ms for all images. The freestream in each image flows from right to left. The cavity is 5 cm (length) x 5.2 cm (depth).

Case 1: Percentage opening area = 100 (No mesh case)

Figure 18 shows the flow visualization for no mesh case at 5 different Reynolds numbers 390, 325, 255, 180 and 100 approximately. In every case, a circulating flow is observed inside the cavity. The centre of circulating flow appeared to move towards upstream direction with decrease in the Reynolds number. Vortex centre can be defined as the region which has maximum vorticity. So only from the vorticity distribution plot, one can decide whether this centre of circulating flow can be called a vortex centre or not. The flow near the top edge of the cavity appeared to be very small. As expected, the flow velocities inside the cavity appeared to decrease with decreasing Reynolds number, which can be visualized from the length of the streaks.

Figure 19 compares the flow field between the cavity and free stream regions, for no mesh case at a Reynolds number of 390. In figure 19(a), the lengths of the streaks in the freestream region are much bigger and so the streak lengths in the freestream region cannot be seen clearly seen. So the exposure time was decreased from 400 ms (Figure 19(a)) to 20 ms (Figure 19(b)). From figure 19(b) one can get a clear picture of the difference in magnitudes of velocity between the two regions. Now it can be seen that the lengths of the streaks in the free stream region are much bigger compared to the cavity region. It can be clearly seen that the length of streaks keep increasing in the free stream as you move away from the intersection of the cavity and the free stream, implying that region is still within the shear layer.

Case 2: Percentage Opening area = 64.8 (Diameter = 0.1905 mm, Rectangle size = 0.7874 mm)

Figure 20 shows the flow visualization for the mesh of 0.1905 mm diameter, 64.8% percentage opening area at 3 different Reynolds numbers 390, 325 and 255. In every case a circulating flow is observed inside the cavity. The centre of the circulating flow appears to be located on the mesh. The centre of the circulation moved upstream as the Reynolds number was decreased. The most significant observation was the huge reduction in the length of streaks inside the cavity region as compared to no mesh case. The velocities near the intersection of the cavity and the free stream appeared less compared to no mesh case. This is due to the hindrance caused by the mesh to the flow.

Case 3: Percentage Opening area = 64.8 (Diameter = 0.1651 mm, Rectangle size = 0.6807 mm)

Figure 21 shows the flow visualization for the mesh of 0.1651 mm diameter, 64.8% percentage opening area at 3 different Reynolds numbers 390, 325 and 255. The characteristics of the flow are similar to previous case. In every case a circulating flow is observed inside the cavity. The centre of the vortex appears to be located on the mesh. Again, the centre of the vortex moved upstream as the Reynolds number is decreased, but this movement was less. The velocities appeared lower compared to previous case, which could be due to the smaller rectangle size. These differences will be described in detail, quantitatively later.

The flow patterns are similar for remaining meshes at all Reynolds number. The lengths of streaks keep decreasing as the percentage opening area decrease.

3.2.2. Measured Quantities

Figure 22 – 26 shows the kinetic energy and vorticity distributions for the no mesh case and one mesh case at Reynolds number of 390. The mean velocity vectors are shown over the total kinetic energy distributions. The distributions are similar at other Reynolds number and also for remaining meshes. The details with regard to pulse width and delay between pulses used for measurements are listed in Table 10-13 in Appendix A. Even though the cavity is of size 5 cm (length) x 5.2 cm (depth) but due to the presence of light reflections very near to the mesh, the results are presented only for 5 cm (length) x 5 cm (depth). The total kinetic energy was calculated using the formula Equation 3.2. Then it

was averaged over the 5 cm (length) x 5 cm (depth) space to get the space averaged total kinetic energy. This space averaged total kinetic energy for every mesh was then normalized with space averaged total kinetic energy of no mesh case at the corresponding Reynolds number to get the normalized space averaged total kinetic energy.

$$\text{Total Kinetic Energy, } TKE = \frac{1}{2}\left(\overline{u}^2 + \overline{v}^2 + (u')^2 + (v')^2\right) \tag{3.2}$$

Kinetic energy distributions based only on mean and fluctuating velocity components are also shown separately. The mean component of total kinetic energy (MKE) and fluctuating component of total kinetic energy (FKE) are given equations 3.3 and 3.4 respectively.

$$\text{Mean component of Total Kinetic Energy, } MKE = \frac{1}{2}\left(\overline{u}^2 + \overline{v}^2\right) \tag{3.3}$$

$$\text{Fluctuating component of Total Kinetic Energy, } FKE = \frac{1}{2}\left((u')^2 + (v')^2\right) \tag{3.4}$$

The normalized space averaged total kinetic energy and normalized average vorticity data for all cases is listed in Table 4.

Case1: Percentage opening area = 100 (No mesh case)

Figure 22 shows the vorticity distribution for both the cavity and freestream. The vorticity distribution looks qualitatively similar at other Reynolds numbers. The vorticity has a maximum value at the corners, near the intersection of the cavity and freestream. The vorticity in the shear region is much larger than the vorticity in the cavity, and there by there is no peak vorticity within the cavity which implies the centre of the circulating flow cannot be termed as vortex centre. The vorticity values keep increasing as one move away from the top edge of cavity except near the side walls. The vorticity is negative near

the side walls and its magnitude is more near the downstream edge of the cavity compared to the upstream edge of the cavity. This is because of large velocity gradients near the downstream edge of the cavity. The magnitudes of vorticity are higher in the half, which is towards the downstream edge of the cavity. Figure 23 (b) shows the vorticity distribution only for the cavity region.

The maximum magnitude of vorticity in the region is 10.09 s^{-1}, 7.71 s^{-1}, 6.82 s^{-1} and average vorticity in the region is 0.53 s^{-1}, 0.46 s^{-1}, 0.39s^{-1} at Reynolds number of 390, 325, and 255 respectively. These average values of no mesh case are used as reference to normalize the vorticity for the cases where the cavity is covered with the mesh, at corresponding Reynolds numbers.

Figure 23(a) shows the total kinetic energy distribution for the no mesh case at Reynolds number of 390. The distribution is not symmetrical about the central axis, which is midway between the upstream and downstream edges of the cavity. The magnitudes of total kinetic energy are higher in the half, which lies towards the downstream edge of the cavity. As expected a circulating flow is observed. The total kinetic energy distribution looks qualitatively similar at other Reynolds numbers too, except that there is a shift in the position of centre of circulating flow. One would expect the region around point x = 2, y = 4.3 in the Figure 23(a), to be the centre of the vortex. But from the vorticity distribution it is seen that the peak vorticity does not lie in that region because of high vorticity in the shear layer.

The maximum value of total kinetic energy is 7.96 mm^2/s^2, 5.34 mm^2/s^2, 3.69 mm^2/s^2 and average value in the region is 0.78 mm^2/s^2, 0.525 mm^2/s^2, 0.34 mm^2/s^2 at a Reynolds number of 390, 325 and 255 respectively. These average values of no mesh case are used as reference to normalize the total kinetic energy for the cases where the cavity is covered with the mesh at corresponding Reynolds numbers. So, the normalized value of total kinetic energy for the no mesh case is 1 at all Reynolds number.

Figure 24(a) shows the mean component of total kinetic energy distribution with mean velocity vectors on top of it. And Figure 24(b) shows the fluctuating component of total kinetic energy distribution with fluctuating component of velocity vectors on top of it. From the distributions it can be seen that the fluctuating component of total kinetic energy is higher near intersection of cavity and freestream, especially towards the downstream edge of the cavity.

The fluctuating component of space averaged total kinetic energy was found to be 1.86%, 2.17%, 2.69% at Reynolds number of 390, 335, and 255 respectively.

Case 2: Percentage Opening area = 64.8 (Diameter = 0.1905 mm, Rectangle size = 0.7874 mm)

Figure 25(b) shows the vorticity distribution at Re ≈ 390. The vorticity is negative in the region near the side walls close to the mesh. The distribution is almost symmetrical about the central axis which is midway between the upstream and downstream edges of the cavity.

The maximum magnitude of vorticity in the region is 2.57 s^{-1}, 1.376 s^{-1}, 0.761 s^{-1} and average vorticity in the region is -0.02s^{-1} (Normalized value = -3.78%), -0.011s^{-1} (Normalized value = -2.33%), -0.0045s^{-1} (Normalized value = -1.17%) at Reynolds number of 390, 325, and 255 respectively.

Even though in this case the flow is circulating in the same direction as the no mesh case, the average vorticity value has opposite sign compared to no mesh case. In no mesh case the large velocity gradients near the intersection of cavity and freestream dominated the velocity gradients near the downstream and upstream edges of cavity. But in the case where the cavity is covered with the mesh, the large velocity gradients are absent near the intersection of cavity and freestream. So, the velocity gradients near the downstream and upstream edges of cavity dominate, making the average vorticity negative.

Figure 25(a) shows the total kinetic energy distribution for the mesh of 0.1905 mm diameter, 64.8% percentage opening area. Its magnitude is high near the corner regions just where it enters and leaves the cavity through the mesh. The distribution is almost symmetrical about the central axis which is midway between the upstream and downstream edges of the cavity.

The maximum value of total kinetic energy is 0.433 mm^2/s^2, 0.118 mm^2/s^2, 0.036 mm^2/s^2 and average value in the region is 0.048 mm^2/s^2 (Normalized value = 6.1%), 0.0122 mm^2/s^2 (Normalized value = 2.33%), 0.0036 mm^2/s^2 (Normalized value = 1.07%) at Reynolds number of 390, 325 and 255 respectively.

Figure 26(a) shows the mean component of total kinetic energy distribution with mean velocity vectors on top of it. And Figure 26(b) shows the fluctuating component of total kinetic energy distribution with fluctuating component of velocity vectors on top of it. From the distributions it can be seen that the fluctuating component of total kinetic energy is higher near intersection of cavity and freestream, especially near the upstream and downstream edges of the cavity.

The fluctuating component of space averaged total kinetic energy was found to be 5.14%, 4.04%, 4.75% at Reynolds number of 390, 335, and 255 respectively. The fluctuating components are relatively higher compared to no mesh case.

Case 3: Percentage Opening area = 64.8 (Diameter = 0.1651 mm, Rectangle size = 0.6807 mm)

Figure 27(a) and 27(b) shows the total kinetic energy and vorticity distribution at Re ≈ 390 respectively. The distribution patterns are qualitatively similar to the above case.

The maximum value of total kinetic energy is 0.223 mm^2/s^2, 0.085 mm^2/s^2, 0.024 mm^2/s^2 and average value in the region is 0.024 mm^2/s^2 (Normalized value = 3.07%), 0.0089 mm^2/s^2 (Normalized value = 1.7%), 0.0013 mm^2/s^2 (Normalized value = 0.38%) at Reynolds number of 390, 325 and 255 respectively.

The fluctuating component of space averaged total kinetic energy was found to be 8.89%, 3.62%, 9.19% at Reynolds number of 390, 335, and 255 respectively. The fluctuating components are relatively higher compared to above two cases.

Case 4: Percentage Opening area = 39.1 (Diameter = 0.1905 mm, Rectangle size = 0.3302 mm)

Figure 28(a) and 28(b) shows the total kinetic energy and vorticity distribution at Re ≈ 390 respectively. The distribution patterns are qualitatively similar to the above case.

Case 5: Remaining meshes

The normalized space averaged total kinetic energy and normalized average vorticity data for all cases is listed in Table 4. The trends are similar for other percentage opening areas. The fluctuating components of space averaged total kinetic energy for all cases are listed in Table 5. The fluctuating components are found to be less than 10% for all the cases, which implies almost steady flow.

3.2.3. Discussion

Figure 29 shows the effect of percentage opening area on normalized space averaged total kinetic energy. It can be clearly seen from the plot that the normalized space averaged total kinetic energy decreases with percentage opening area at all Reynolds numbers. The normalized space averaged total kinetic energy decreases with decrease in Reynolds number at all percentage opening areas.

By covering the cavity surface with a mesh of 0.1905 mm diameter, 64.8% percentage opening area, the normalized space averaged total kinetic energy decreased to 6.04%, 2.3%, and 1.07% at Reynolds number of 390, 325 and 255 respectively. This shows how rapidly the normalized values decrease with decrease in percentage opening area, which implies the slope of the curves will be too large at percentage opening areas greater than 64.8%. At 64.8% opening area the slope of curve at Reynolds number of 390 and 325 already started growing rapidly, but relatively the slope of the curve at Reynolds number of 255 is less.

At 64.8% two data sets can been seen and they don't overlap on each other. This is because those meshes are of different diameters and rectangle sizes. The comparison between those two meshes will be discussed in the next section.

The fluctuating component of space averaged total kinetic energy is calculated to be less than 10% for all cases. From fluctuating component calculations, it is seen that the effect of percentage opening area on the fluctuating components has no particular trend.

As mentioned previously, the results will be compared with the aneurysm result of Chee Lum (2007). The stent used in that experiment has a diameter of 5 mm and the wire thickness of it is 0.1077 mm. The aneurysm opening was 6.5 mm wide and the percentage opening area of the stent was 80%. The normalized total kinetic energy decreased to 9.6% (Figure 3) when the aneurysm opening was covered with the stent. This experiment was done at Reynolds number of 184 (based on tube diameter) and 267

(based on aneurysm opening diameter). But, he calculated the total kinetic energies based on only mean velocities (equation 3.3). So in Figure 30 the mean components of space averaged total kinetic energies are compared with the aneurysm result.

As mentioned before the slope of the curve at Re of 255 is relatively less at 64.8%, so by looking at trends the slope for a curve at Re of 184 will be less at this percentage opening area. The result from the brain aneurysm experiment doesn't quite fit on these curves. From the trends it appears that at 80% opening area the normalized space averaged total kinetic energy on the curve, Re = 184 will be less than the value from aneurysm experiment. But if Re of the aneurysm experiment is considered as 267 then there appears a high probability for the aneurysm experiment result to follow the trends of rectangular cavity experiment results.

It is assumed that the fluctuation component of space averaged total kinetic energy in the aneurysm experiment is small, which implies trends will be similar even if one were to compare the aneurysm result and rectangular cavity results based on space averaged total kinetic energies and not just its mean components.

As mentioned in the previous chapter the settling speed of silver coated hollow spheres is 0.124mm/s for a particle of diameter 19.5μm and density 1.6g/cc. The settling speed is more or less equivalent to the peak speed in the cavity for extremely low percentage opening area meshes especially at Re of 263. So this phenomenon could have affected the result at very low speeds. But since the diameters of the particles range between 6μm and

32μm and similarly the particle density is also distributed and not exactly 1.6g/cc, so there will always be particles whose settling speeds are very low and hence their trajectories are not influenced by their settling speed. Whenever new particles were added to the flow, atleast 30 min was given for the water tunnel to come to a steady state. And while changing speeds, atleast 10 - 15 min was given for the water tunnel to settle. During that period of time, the denser particles would have settled down. So settling speed issue would not affect the results very much.

Table 4. Normalized space averaged total kinetic energy data from the study of variation in percentage opening area and rectangle size

Mesh properties				Water tunnel frequency = 6hz, Re ≈ 255		Water tunnel frequency = 8hz, Re ≈ 325		Water tunnel frequency = 10hz, Re ≈ 390	
Diameter (mm)	Percentage opening area	Rectangle size (mm)	Dimensionless Rectangle size	Normalized TKE	Normalized Vorticity	Normalized TKE	Normalized Vorticity	Normalized TKE	Normalized Vorticity
0.1397	49.4	0.3302	0.0660	0.1527	-0.8374	0.2756	-1.4603	0.1703	-1.0882
0.1397	59.1	0.4572	0.0914	0.3848	-0.7094	0.8029	-1.9002	1.0794	-2.4161
0.1651	37.2	0.2540	0.0508	0.0368	-0.7270	0.0645	-0.8106	0.1104	-1.1979
0.1651	56.7	0.5080	0.1016	0.2450	-1.6887	0.4686	-1.4817	0.7578	-2.5236
0.1651	64.8	0.6807	0.1361	0.3818	-1.8901	1.7042	-1.3751	3.0712	-3.9917
0.1905	39.1	0.3302	0.0660	0.0936	-0.6668	0.1495	-1.0952	0.2512	-1.4306
0.1905	64.8	0.7874	0.1575	1.0709	-1.1735	2.3295	-2.3932	6.0977	-3.7844
No mesh case				100	100	100	100	100.0000	100

Table 5. Fluctuating component of space averaged TKE data from the study of variation in percentage opening area and rectangle size

Mesh properties				Fluctuating component of TKE (%)		
Diameter (mm)	Percentage opening area	Rectangle size (mm)	Dimensionless Rectangle size	Water tunnel frequency = 6hz, Re ≈ 255	Water tunnel frequency = 8hz, Re ≈ 325	Water tunnel frequency = 10hz, Re ≈ 390
0.1397	49.4	0.3302	0.0660	8.8799	4.9433	4.1659
0.1397	59.1	0.4572	0.0914	4.7330	4.4033	3.6697
0.1651	37.2	0.2540	0.0508	5.9231	8.2570	9.5403
0.1651	56.7	0.5080	0.1016	7.1794	7.5772	10.4049
0.1651	64.8	0.6807	0.1361	9.1904	3.6258	8.8884
0.1905	39.1	0.3302	0.0660	6.2453	5.1975	4.3913
0.1905	64.8	0.7874	0.1575	4.7526	4.0376	5.1352
No mesh case				2.6915	2.1714	1.8629

3.3. Results of effect of rectangle size of mesh

Cavity opening length of 0.5 cm is used to normalize the rectangle size for the rectangular cavity experiments. For the aneurysm, the cavity opening diameter is about 0.65 cm whose equivalent rectangular cavity opening length is 0.576 cm. The meshing structure was not rectangle in the aneurysm. So based on the percentage opening area (80%) and diameter of the wire (0.1077mm) in the stent, the equivalent rectangle size was estimated as 0.9124mm. The normalized rectangle size of the aneurysm was calculated to be 0.1584 after normalizing with 0.576 cm.

The numerical data for the effect of normalized rectangle size on normalized space averaged total kinetic energy is shown in Table 4. This is the same data that has been used to study the effect of percentage opening area on normalized space averaged TKE.

3.3.1. Discussion

Figure 31 shows the effect of normalized rectangle size on normalized space averaged total kinetic energy. It can be seen that normalized space averaged total kinetic energy decreases with decrease in normalized mesh size. This trend is not followed at a normalized mesh size of 0.091 and 0.102. The values of normalized space averaged total kinetic energy are larger at a normalized mesh of 0.091 compared to the values at 0.102 for all Reynolds numbers. This could be because of higher percentage opening area of 59.1% for a mesh size of 0.091 case compared to 56.7% for a mesh size of 0.102.

In the previous section it is seen that the meshes with same percentage opening area (64.8%) do not have the same normalized space averaged total kinetic energy at all three Reynolds numbers. For the case with normalized rectangle size of 0.157, the normalized space averaged total kinetic energy was 6.09%, 2.3%, and 1.07% and for the case with normalized rectangle size of 0.136, the normalized space averaged total kinetic energy was 3.07%, 1.7%, 0.38% at Reynolds number of 390, 325 and 255 respectively. This difference in normalized rectangle size should be the cause for the difference in normalized space averaged total kinetic energy.

The positioning of mesh with respect to cavity could have also affected the result. The details about the effect of positioning of mesh will be discussed in the next section. For the case of rectangle size 0.157, the first wire of the mesh is a bit far away from the downstream edge of the cavity, compared to the mesh whose rectangle size is 0.136. But here the meshes are of different rectangle size and diameter, so it's not easy to compare this positioning of mesh effect in these meshes.

As mentioned before for comparing the rectangular cavity results with aneurysm result, only mean component of space averaged total kinetic energy has to be considered. Figure 32 shows the effect of normalized rectangle size of mesh on normalized mean component of space averaged total kinetic energy inside the cavity. Even in this plot the aneurysm data point doesn't follow the trend of rectangular cavity experiment results. From the trends it is very clear that at 80% opening area the normalized space averaged TKE on

both the curves, Re of 184 and Re of 267 will be definitely less than the value from aneurysm experiment.

This difference could be because of few differences between the experiments. In rectangular cavity experiment, the edges of cavity are perpendicular to the freestream direction while the edges are round in the brain aneurysm experiment. Secondly, the cavity is rectangular compared to almost circular in the aneurysm experiment. Thirdly, the flow in the rectangular cavity experiment is open cavity type compared to pipe flow type in the aneurysm experiment. Fourthly, the mesh used in the rectangular cavity experiment is rectangular in nature compared to a different shape of stent (Figure 1) in the aneurysm experiment. Fifthly, the flow is nominally 2-dimensional in nature in rectangular cavity experiment compared to 3-D in aneurysm experiment.

3.4. Results for effect of positioning of mesh

The mesh used for this part of experiment has a diameter of 0.1905mm, 64.8% percentage opening area and rectangle size of 0.7874mm. In the 2 cases, the Reynolds number varies slightly by 10 – 20 at all three Reynolds number. Except positioning of mesh, remaining experimental setup was maintained same. The discussion will be done only for Re ≈ 390. Similar patters are seen at other Reynolds numbers too.

3.4.1 Flow Visualization

Figure 33 shows the flow visualization of the effect of position of mesh with respect to cavity at a Reynolds numbers of ≈ 390. Inside the cavity region, the first wire of the mesh is closer to the downstream edge of the cavity in the figure 33(b) compared to figure 33(a). The length of the streaks in the region near to downstream edge of the cavity is smaller in figure 33(b) compared to figure 33(a). So it appears there is less amount of total kinetic energy inside the cavity for the case where first wire of mesh is closer to downstream edge of the cavity.

3.4.2 Measured Quantities

Case 1: First wire of the mesh at a distance of ≈ 0.7 mm from the downstream edge of cavity

Figure 34(a) shows the total kinetic energy distribution for the case whose first wire is at a distance of ≈ 0.7 mm for Reynolds number of ≈ 390. Its magnitude is high near the corner regions just where it enters and leaves the cavity through the mesh. The

distribution is almost symmetrical about the central axis which is midway between the upstream and downstream edges of the cavity.

The maximum value of total kinetic energy is 0.433 mm^2/s^2, 0.118 mm^2/s^2, 0.036 mm^2/s^2 and average value in the region is 0.048 mm^2/s^2 (Normalized value = 6.1%), 0.0122 mm^2/s^2 (Normalized value = 2.33%), 0.0036 mm^2/s^2 (Normalized value = 1.07%) at Reynolds number of 390, 325 and 255 respectively.

Figure 34(b) shows the vorticity distribution at Re ≈ 390. The vorticity is negative in the region near the side walls close to the mesh. The distribution is almost symmetrical about the central axis which is midway between the upstream and downstream edges of the cavity.

The maximum magnitude of vorticity in the region is 2.57 s^{-1}, 1.376 s^{-1}, 0.761 s^{-1} and average vorticity in the region is -0.02s^{-1} (Normalized value = -3.78%), -0.011s^{-1} (Normalized value = -2.33%), -0.0045s^{-1} (Normalized value = -1.17%) at Reynolds number of 390, 325, and 255 respectively.

Case 2: First wire of the mesh at a distance of ≈ 0.2 mm from the downstream edge of cavity

Figure 35(a) and 35(b) shows the total kinetic energy distribution and vorticity distribution for the case whose first wire is at a distance of ≈ 0.2 mm for Reynolds number of 384.4 respectively.

The maximum value of total kinetic energy is 0.204 mm^2/s^2, 0.01 mm^2/s^2, 0.036 mm^2/s^2 and average value in the region is 0.019 mm^2/s^2 (Normalized value = 2.4%), 0.008 mm^2/s^2 (Normalized value = 1.54%), 0.003 mm^2/s^2 (Normalized value = 0.89%) at Reynolds number of 384.4, 316.6 and 245.5 respectively.

The maximum magnitude of vorticity in the region is 1.4 s^{-1}, 1.225 s^{-1}, 0.818 s^{-1} and average vorticity in the region is -0.019s^{-1} (Normalized value = -3.78%), -0.008s^{-1} (Normalized value = -1.753%), -0.0043s^{-1} (Normalized value = -1.11%) at Reynolds number of 384.4, 316.6 and 245.5 respectively.

3.4.3 Discussion

Figure 36 shows results for effect of positioning of mesh with respect to cavity. The ratio of normalized total kinetic energies at 10 Hz frequency of motor for Case A and B (Re = 390 for Case 1, Re = 384.4 for Case 2) is 2.54.

In no mesh case (Figure 18) the region (1.4 mm from the downstream edge of the cavity) very close to the downstream edge of the cavity has regions of high total kinetic energy. In figure 33(b) both the first and second wires were present in this region of high total kinetic energy. But in figure 33(a) only the first wire was present in this region. Considering only a length of 1.4 mm from the downstream edge of the cavity, the local percentage opening area for case 33(a) is calculated to be 69.6% and 58.61% for case 33(b). Since the experiment setups for both the cases were same except the positioning of

mesh with respect to cavity, this was the only reason that could explain the reason behind decrease in normalized space averaged total kinetic energy.

3.5. Results of effect of exposed length of mesh

The mesh used for this part of experiment has a diameter of 0.1905mm, 64.8% percentage opening area and rectangle size of 0.7874mm. A mesh of length 6 cm is symmetrically placed with respect to the cavity. The length of the mesh that is exposed to the flow has been varied using a black tape and the effect of this exposed length on the cavity flow has been studied in the next two subsections. Figure 9(b) shows the schematic for this part of the experiment. Altogether 5 different exposed lengths namely 2 cm, 1 cm, 0.5 cm, 0.2 cm and 0 cm have been studied. The exposed length is defined as the length of mesh exposed to the flow, upstream to the upstream edge of the cavity. Except exposed length of the mesh, remaining experimental setup was maintained same.

3.5.1 Flow Visualization

Figure 37(a) and (b) shows the particle streak flow visualization for exposed lengths of 0 cm and 2 cm respectively. In a movie sequence it is observed that for remaining 3 cases, the flow is a lot unsteady in nature and so particle streak flow visualization images aren't shown. The flow patterns are described only Re $\approx$ 390. The flow patterns are similar at other Reynolds numbers too.

Case 1: Exposed length = 0 cm

Figure 37(a) shows the flow visualization for the case where exposed length is 0 cm. The flow direction is clockwise inside the cavity.

Case 2: Exposed length = 2 cm

Figure 37(b) shows the flow visualization for the case where exposed length is 2 cm. The flow direction is anti-clockwise inside the cavity. This flow pattern was opposite to previous case (exposed length = 0) where the flow direction is clockwise. The only reason to explain this flow behavior is because of the exposure to 2 cm of mesh length upstream to the upstream edge of the cavity. In this case the flow is flowing over a rugged surface (because the mesh is exposed to flow), compared to smooth surface (because of presence of black tape) in the case of zero exposure length. The mechanism which caused this flow pattern is not yet known.

Case 3: Exposed length = 1 cm and 0.5 cm

From movie sequence of these flow visualizations, the flow inside the cavity is observed to be unsteady in nature. So the flow visualizations were not presented. The flow direction inside the cavity kept changing from clockwise to counterclockwise, but for most part of the time the direction was counterclockwise in direction. This shows that the flow direction is slowly transforming from counterclockwise direction to clockwise direction with decrease in exposed lengths.

At an exposed length of 1 cm, the flow appeared unrealistic. This is because the fluid entering and fluid leaving the mesh does not appear to balance. The fluid leaving the mesh appears to be a lot more compared to fluid entering the mesh. Probably the flow has become 3D in nature.

Case 4: Exposed length = 0.2 cm

Even for this case the flow observed was unsteady in nature. So the flow visualization was not presented. The velocities appeared to be very low because of small streak lengths. The flow direction pattern kept changing very rapidly. It appears that the critical point for the flow direction pattern to change from counterclockwise to clockwise pattern appears to be around 0.2 cm of exposed length.

3.5.2 Measured Quantities

Table 6 shows the numerical quantities for effect of exposed length of mesh on normalized space averaged total kinetic energy at all three speeds. Figure 38, 39 shows the total kinetic energy and vorticity distributions for an exposure lengths of 0 and 2 cm respectively at a motor frequency of 10hz (Re $\approx$ 390). Table 7 shows the fluctuating component of space averaged total kinetic energy for all the five cases at all three Reynolds numbers. The fluctuations are as high 70% for the exposed lengths of 0.5 cm and 0.2 cm. This show how unsteady the flow patterns are inside the cavity.

3.5.3 Discussion

From the movie sequences of particle streak flow visualizations it is observed that the flow direction inside the cavity changes from counterclockwise to clockwise as the exposed length is decreased.

Figure 40 shows the effect of exposed length of mesh on the flow field. For a water tunnel motor frequency of 10 Hz, the normalized space averaged total kinetic energy decreased from 1.397% to 0.3% as the exposed length decreased from 2 cm to 0.5 cm and then later it increased from 0.3% to 6.09% as the exposed length decreased from 0.5 cm to 0 cm. Almost similar trends are observed for the other two Reynolds number.

From the numerical results it can be seen that the critical length (defined as the length where the normalized space averaged total kinetic energy is minimum) could be between an exposed lengths of 0.2 to 0.5 cm. The critical length could vary with variation in Reynolds number. To find this out, data have to be collected for every 0.1 cm of exposed length and to see a large difference in the position of critical point, the Reynolds number range has to be increased.

Table 6. Normalized space averaged total kinetic energy data from the study of effect of exposed length of mesh

Mesh – 0.1905 mm diameter, 64.8% opening area, 0.7874 mm rectangle size									
Exposed length (cm)	Water tunnel frequency = 6hz			Water tunnel frequency = 8hz			Water tunnel frequency = 10hz		
	Re	Normalized TKE	Normalized Vorticity	Re	Normalized TKE	Normalized Vorticity	Re	Normalized TKE	Normalized Vorticity
0	255.00	1.07	-1.17	325.00	2.32	-2.39	390.00	6.09	-3.78
0.2	261.80	0.15	0.46	325.90	0.17	0.28	413.05	0.45	0.89
0.5	251.70	0.15	1.09	331.75	0.31	2.41	395.95	0.29	1.63
1.0	245.25	0.26	0.83	325.10	0.40	1.26	367.75	1.03	3.81
2.0	257.65	0.43	1.45	330.70	0.82	3.05	390.00	1.39	4.99
No mesh case	255.00	100	100	325.00	100	100	390.00	100	100

Table 7. Fluctuation component of normalized space averaged TKE data from the study of effect of exposed length of mesh

Mesh – 0.1905 mm diameter, 64.8% opening area, 0.7874 mm rectangle size						
Exposed length (cm)	Water tunnel frequency = 6hz		Water tunnel frequency = 8hz		Water tunnel frequency = 10hz	
	Re	Fluctuation component %	Re	Fluctuation component %	Re	Fluctuation component %
0	255.00	4.75	325.00	4.03	390.00	5.13
0.2	261.80	70.75	325.90	33.21	413.05	41.80
0.5	251.70	69.17	331.75	29.00	395.95	71.68
1.0	245.25	38.63	325.10	32.21	367.75	22.46
2.0	257.65	21.60	330.70	21.47	390.00	13.18
No mesh case	255.00	2.69	325.00	2.17	390.00	1.86

3.6. Results of effect of gap between the mesh and cavity

The mesh used for this part of experiment has a diameter of 0.1905mm, 64.8% percentage opening area and rectangle size of 0.7874mm. A mesh of length 2 cm is symmetrically placed over the stainless steel shim stocks. The thickness of the shimstocks has been varied and the effect of the gap between the cavity and mesh, on the cavity flow has been studied in the next two subsections. Figure 10 shows the schematic for this part of the experiment. Altogether 3 different gaps namely 0.127 mm, 0.254 mm and 0.508 mm have been studied. Except the gap, remaining experimental setup was maintained same. Since the mesh was not perfectly flat, maintaining desired gap between the mesh and cavity was a bit difficult.

3.6.1 Flow Visualization

Figure 41 (a), (b), (c) shows the flow visualization for gaps of 0.508 mm, 0.254 mm and 0 mm respectively. The flow pattern for a gap of 0.254 mm is similar to the case where the gap is 0.508 mm. The flow patterns are described only for 10 Hz frequency of the water tunnel motor (Re $\approx$ 390).

Case 1: Gap = 0.508 mm

Figure 41 (a) shows the flow visualization for a gap of 0.508 mm. The flow inside the cavity is counterclockwise in nature. The flow enters the cavity from the gap on the right bottom side of the cavity and it leaves though the gap on the left bottom side of the cavity and also through the mesh. The flow in the bottom half of the cavity was a lot faster compared to upper half implying large velocity differences between the 2 halves. The

flow pattern was similar at other Reynolds numbers too. Only for Reynolds number of 392 a very slow circulating flow was seen on top right corner of the cavity.

Case 2: Gap = 0.127 mm

Figure 41 (b) shows the flow visualization for a gap of 0.127 mm. The flow pattern for this gap was different compared to previous gap cases. For this case two types of flow patterns are observed. The flow inside the cavity is counterclockwise in the right half of the cavity and clockwise in the left half of the cavity. The flow enters the cavity from the gap on the right bottom side of the cavity and also enters from the left bottom corner of the cavity through the mesh and it leaves though the through the middle cells of the mesh. This different flow pattern could be because the gap was so low that the mesh might have touched the surface of the flat plate on the downstream side of the cavity.

Case 3: Gap = 0 mm

Figure 41 (c) shows the flow visualization for zero gap case. The flow inside the cavity is from clockwise in nature.

Case 4: Gap = 0.254 mm

The flow pattern was similar to the case where gap was 0.508 mm. The flow inside the cavity is counterclockwise in nature. The flow enters the cavity from the gap on the right bottom side of the cavity and it leaves though the gap on the left bottom side of the cavity and also through the mesh. The flow in the bottom half of the cavity was a lot faster compared to upper half

3.6.2 Measured Quantities

Table 8 shows the numerical quantities for the effect of gap between the mesh and cavity on normalized space averaged total kinetic energy at all three speeds. Table 9 gives the fluctuating components of normalized space averaged total kinetic energy. The fluctuations are less 10% for all cases.

Case 1: Gap = 0.508mm

Figure 42(a) and 42(b) shows the total kinetic energy and vorticity distribution respectively, for a gap size of 0.508 mm at Reynolds number of 392.7. The distribution patterns are almost similar at other Reynolds numbers too. Figure 45 shows that the normalized space averaged total kinetic energy decreased with decrease in Reynolds number for the gap of 0.508 mm. Similar patters are observed for gap of 0.254 mm.

Case 2: Gap = 0.127mm

Figure 43(a) and 43(b) shows the total kinetic energy and vorticity distribution respectively, for a gap size of 0.127 mm at Reynolds number of 406. The distribution patterns are almost similar at other Reynolds numbers too. Figure 45 shows that the normalized space averaged total kinetic energy increased with decrease in Reynolds number for the gap of 0.127 mm. But the total kinetic energy decreased with decrease in Reynolds number.

Case 3: Gap = 0mm

Figure 44(a) and 44(b) shows the total kinetic energy and vorticity distribution respectively, for a gap size of 0mm at Reynolds number of 384. The distribution patterns are almost similar at other Reynolds numbers too. Figure 45 shows that the normalized space averaged total kinetic energy decreased with decrease in Reynolds number for the gap of 0 mm.

3.6.3 Discussion

From particle streak flow visualizations it was clearly seen that the flow direction inside the cavity changes from clockwise to counterclockwise as the gap between the cavity and mesh was increased. For no mesh case the flow pattern was clockwise, which implies as the gap is still increased the flow direction changes back to clockwise. Figure 45 shows the effect of gap on normalized space averaged total kinetic energy at all three Reynolds numbers.

For a Reynolds number of ≈ 390, the normalized space averaged total kinetic energy has decreased from 2.4% to 1.4% as the gap was increased from 0mm to 0.127 mm and then it increased from 1.4% to 15.23% as the gap increased from 0.127 mm to 0.508 mm.

The normalized space averaged total kinetic energy is highest for a gap of 0.508 mm at all three Reynolds numbers. The normalized space averaged total kinetic energy is higher at 0.254mm and 0mm gap compared to 0.127mm gap at water tunnel motor frequencies

of Re ≈ 390 and Re ≈ 325. But at Re ≈ 255 the case with 0.127mm gap has higher total kinetic energy compared to 0.254mm and 0mm gap.

The normalized space averaged total kinetic energy decreased with decrease in Reynolds number at gaps except for the case with gap 0.127 mm. The normalized space averaged total kinetic energy increased with decrease in Reynolds number for the gap of 0.127 mm. But the total kinetic energy decreased with decrease in Reynolds number at this gap.

Table 8. Normalized space averaged total kinetic energy data for the study of effect of gap between the mesh and the cavity opening

Mesh – 0.1905 mm diameter, 64.8% opening area, 0.7874 mm rectangle size									
Gap (mm)	Water tunnel frequency = 6hz			Water tunnel frequency = 8hz			Water tunnel frequency = 10hz		
	Re	Normalized TKE	Normalized Vorticity	Re	Normalized TKE	Normalized Vorticity	Re	Normalized TKE	Normalized Vorticity
0	245.50	0.8878	-1.1104	316.65	1.5242	-1.7533	384.41	2.3974	-3.6091
0.127	261.57	2.3662	-2.8257	338.58	1.7139	-2.4869	406.19	1.8936	-1.9186
0.254	246.80	1.4009	7.7663	318.80	2.6724	12.7114	393.35	6.9531	14.8549
0.508	245.75	3.8534	17.9007	321.15	8.9448	30.5580	392.70	15.2282	44.7606
No mesh case	255.00	100	100	325.00	100	100	390.00	100	100

Table 9. Fluctuation component of normalized space averaged TKE data from the study of effect of gap between the mesh and the cavity opening

Mesh – 0.1905 mm diameter, 64.8% opening area, 0.7874 mm rectangle size						
Gap (mm)	Water tunnel frequency = 6hz		Water tunnel frequency = 8hz		Water tunnel frequency = 10hz	
	Re	Fluctuation component %	Re	Fluctuation component %	Re	Fluctuation component %
0	245.50	5.0696	316.65	4.1365	384.41	7.2853
0.127	261.57	9.8520	338.58	4.5499	406.19	8.2579
0.254	246.80	6.7640	318.80	6.2680	393.35	8.1353
0.508	245.75	5.8151	321.15	3.8075	392.70	3.8287
No mesh case	255.00	2.6915	325.00	2.1714	390.00	1.8629

4. CONCLUSION

Characterized the changes in the recirculation flow pattern inside the cavity caused by a porous surface (rectangular mesh) covering the cavity opening. The effect of several parameters namely, percentage opening area, rectangle size, length of mesh, positioning of mesh with respect to cavity and also effect of gap between mesh and cavity on the cavity flow field have been studied using digital particle image velocimetry technique.

At 1.8cm upstream to the upstream edge of the cavity the boundary layer thickness is measured to be 0.74cm, 0.774cm, 0.851cm for Reynolds numbers of 378.49 (U_0 = 7.57 cm/s), 325.1 (U_0 = 6.5 cm/s), and 251.56 (U_0 = 5.031 cm/s) respectively.

A circulating flow pattern is observed inside the cavity for no mesh case and the centre of circulating flow moved towards upstream direction with decrease in the Reynolds number. The most significant finding is the huge reduction in total kinetic energy when the cavity opening was covered with the mesh for all cases.

Even though the cavity is of size 5 cm (length) x 5.2 cm (depth) but due to the presence of light reflections very near to the mesh, the results are presented only for 5 cm (length) x 5 cm (depth). The results will vary by few percentages because data analysis is done only up to a depth of 5 cm. In all calculations the space averaged total kinetic energies and vorticity are normalized by the corresponding no mesh case values. Since the values of total kinetic energy and vorticity are high in region between depth of 5 cm and 5.2 cm,

all the normalized values are estimated slightly high. So choice of region for averaging will affect the results slightly.

A clockwise flow pattern is observed inside the cavity, when the cavity is covered with the mesh for all cases. The normalized space averaged total kinetic energy decreased with decrease in percentage opening area at all Reynolds numbers. The normalized space averaged total kinetic energy decreased with decrease in Reynolds number at all percentage opening areas. At 64.8% two data sets can been seen and they don't over lap on each other. This is because those meshes are of different diameters and rectangle sizes. Numerical results showed that the fluctuating component of space averaged total kinetic energy is high near the corners close to downstream and upstream edges of cavity (near the intersection of cavity and freestream).

It was seen that normalized space averaged total kinetic energy decreases with decrease in normalized mesh size. This trend is not followed at a normalized mesh size of 0.091 and 0.102. The values of normalized space averaged total kinetic energy are larger at a normalized mesh of 0.091 compared to the values at 0.102 for all Reynolds numbers. This could be because of higher percentage opening area of 59.1% for a mesh size of 0.091 case compared to 56.7% for a mesh size of 0.102.

The result from the brain aneurysm experiment doesn't follow the trend of rectangular cavity experiment results (normalized mean component of space averaged total kinetic energy vs percentage opening area & normalized mean component of space averaged

kinetic energy vs normalized rectangle size) if the Re for aneurysm experiment is assumed to be 184. This is because of few differences between the experiments as explained in previous chapters. But if Re = 267, then the aneurysm result appears to follow the trend of rectangular cavity experiment results when TKE is plotted against percentage opening area.

It is observed that the positioning of mesh with respect to cavity affects the cavity flow field. The closer the first wire of the mesh to the downstream edge of the cavity, the lesser is the normalized space averaged total kinetic energy. This is because the local percentage opening area very near to the downstream edge of the cavity becomes lesser.

From flow visualizations it is clearly seen that the flow direction inside the cavity changes from counterclockwise pattern to clockwise pattern as the exposed length was decreased. From the numerical results it is seen that the normalized space averaged total kinetic energy decreased as the exposed the length decreased from 2 cm to 0.2 cm, but then the normalized space averaged total kinetic energy drastically increased when the exposed length was decreased from 0.2 cm to 0 cm. This shows that the critical length is around an exposed length of 0.2 cm. The critical length could vary with variation in Reynolds number. From movie sequences of particle streak flow visualization it is observed that at the point of critical length the flow is unsteady in nature. The fluctuation component of space averaged total kinetic energy increased with increase in exposed length. As this exposed length is increased beyond the critical length, the fluctuations will decrease.

From flow visualizations it was clearly seen that the flow direction inside the cavity changes from clockwise pattern to counterclockwise pattern as the gap between the cavity and mesh was increased. For no mesh case the flow pattern was again clockwise, which implies as the gap keeps increasing the flow direction changes back to clockwise. The experimental results showed that the normalized space averaged total kinetic energy is highest for a gap 0.508mm at all three Reynolds numbers. The normalized space averaged total kinetic energy is higher for at 0.254mm and 0mm gap compared to 0.127mm gap at water tunnel motor frequencies of 10 Hz and 8 Hz. But at 6 Hz the case with 0.127mm gap has higher total kinetic energy compared to 0.254mm and 0mm gap.

From the qualitative and quantitative analysis, it was found that for any chosen mesh the total kinetic energy inside the rectangular cavity can be decreased by 2 methods. First method was to have the first wire of the mesh as close as possible to the downstream edge of the cavity and second method was to have the length of mesh exposed to the flow to be critical length. Unless experiments are done on aneurysm, it is difficult to say whether the two proposed methods will be able to reduce the total kinetic energy inside the aneurysm or not, because of the difference in experimental setups.

APPENDIX A

Table 10. Timing data for the study of effect of percentage opening area and rectangle size

Mesh properties				Water tunnel frequency = 6hz, Re ≈ 255		Water tunnel frequency = 8hz, Re ≈ 325		Water tunnel frequency = 10hz, Re ≈ 390	
Diameter (mm)	% opening area	Rectangle size (mm)	Cell per inch	Pulse delay (ms)	Pulse width (ms)	Pulse delay (ms)	Pulse width (ms)	Pulse delay (ms)	Pulse width (ms)
0.1397	49.4	0.3302	54 x 54	400	28	300	22	200	18
0.1397	59.1	0.4572	42 x 42	200	14	140	10	80	5
0.1651	37.2	0.2540	60 x 60	700	30	500	30	300	25
0.1651	56.7	0.5080	38 x 38	300	8	180	7	120	6
0.1651	64.8	0.6807	30 x 30	130	4	90	4	65	4
0.1905	39.1	0.3302	50 x 50	900	50	500	40	300	30
0.1905	64.8	0.7874	26 x 26	150	10	100	8	50	4
No mesh case				23	2.5	18	2	15	2

Table 11. Timing data for the study of effect of exposed length of mesh

Mesh – 0.1905 mm diameter, 64.8% opening area, 0.7874 mm rectangle size									
Exposed length (cm)	Water tunnel frequency = 6hz			Water tunnel frequency = 8hz			Water tunnel frequency = 10hz		
	Re	Delay between pulses (ms)	Pulse width (ms)	Re	Delay between pulses (ms)	Pulse width (ms)	Re	Delay between pulses (ms)	Pulse width (ms)
0	255.00	150	10	325.00	100	8	390.00	50	5
0.2	261.80	300	10	325.90	300	10	413.05	200	8
0.5	251.70	300	10	331.75	200	8	395.95	50	5
1.0	245.25	150	10	325.10	100	8	367.75	50	5
2.0	257.65	150	10	330.70	100	8	390.00	50	5
No mesh case	255.00	23	2.5	325.00	18	2	390.00	15	2

Table 12. Timing data for the study of effect of gap between the mesh and the cavity opening

Mesh – 0.1905 mm diameter, 64.8% opening area, 0.7874 mm rectangle size									
Gap (mm)	Water tunnel frequency = 6hz			Water tunnel frequency = 8hz			Water tunnel frequency = 10hz		
	Re	Delay between pulses (ms)	Pulse width (ms)	Re	Delay between pulses (ms)	Pulse width (ms)	Re	Delay between pulses (ms)	Pulse width (ms)
0	245.50	150	10	316.65	100	8	384.40	50	5
0.127	261.57	80	8	338.58	60	6	406.19	40	4
0.254	246.80	80	10	318.80	60	8	393.35	40	5
0.508	245.75	50	6	321.15	35	4	392.70	20	2
No mesh case	255.00	23	2.5	325.00	18	2	390.00	15	2

Table 13. Water Tunnel Calibration

Water tunnel frequency (Hz)	Delay between pulses (ms)	Pulse width (ms)	Freestream Velocity (cm/s)	Reynolds number		Water Tunnel Frequency (Hz)	Delay between pulses(ms)	Pulse width (ms)	Freestream Velocity (cm/s)	Reynolds number
2	20	0.7	2.02	100.86		11	4.5	0.5	8.72	436.08
3	17	0.7	2.91	145.4		12	4	0.5	9.45	472.56
4	14	0.7	3.58	179.12		13	3.5	0.5	10.08	503.92
5	11	0.7	4.73	236.25		14	3.5	0.45	11.09	554.68
6	8	0.7	5.28	255.87		15	3.5	0.45	11.62	581.02
7	5	0.7	5.9	295.09		16	3.5	0.45	12.01	600.93
8	5	0.6	6.75	325.62		17	3.5	0.45	12.42	621.09
9	5	0.5	7.35	367.87		18	3	0.425	13.22	661.13
10	5	0.5	7.94	390.93						

APPENDIX B

```
interest_piv -d 15 -c 41 -s 61 -x 48,1098 -y 0,932 0 0 seq.in

seq_corr -o seq.out -a 10f_003.tif 123 < seq.in

seq2tec seq.out tec.dat

seq_dice -Q 0.75 -R 255646787,0,0 -x 48,1098 -y 0,200 seq.out seq_dice1.out

seq2tec seq_dice1.out tec_dice1.dat

seq_dice -Q 2 -R 255646787,0,0 -x 48,1098 -y 200,400 seq.out seq_dice2.out

seq2tec seq_dice2.out tec_dice2.dat

seq_dice -Q 5 -R 255646787,0,0 -x 48,1098 -y 400,600 seq.out seq_dice3.out

seq2tec seq_dice3.out tec_dice3.dat

seq_dice -Q 9 -R 255646787,0,0 -x 48,1098 -y 600,932 seq.out seq_dice4.out

seq2tec seq_dice4.out tec_dice4.dat

combine_bin seq_dice1.out seq_dice2.out seq_dice3.out seq_dice4.out seq_dice.out

seq2tec seq_dice.out tec_dice.dat

rm_bad -l 1 -p 2 -z seq_dice.out seq_rm.out

seq2tec seq_rm.out tec_rm.dat

make_off > scale.txt

seq_scale seq_rm.out seq_scale.out < scale.txt

seq2tec seq_scale.out tec_scale.dat

irreg2reg -x -0.1, 0.1,5 -y 0, 0.1,5 -2 -w 8 -W wall_file.dat seq_scale.out seq_reg.out

seq2tec seq_reg.out tec_reg.dat
```

```
seq_avg seq_reg.out seq_avg.out seq_rms.out

seq2tec seq_avg.out tec_avg.dat

seq2tec seq_rms.out tec_rms.dat
```

APPENDIX C

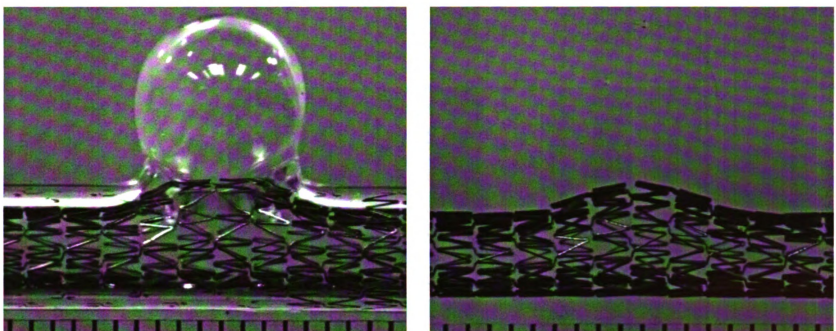

(a) (b)

Figure 1. Optical matching of aneurysm model (a) without optical matching (b) with optical matching. Inner diameter of tube = 4 mm; aneurysm cavity opening = 6.5 mm; diameter of the stent = 5 mm, but = 4 mm when placed inside the tube (since it gets compressed and takes the shape of tube)

(a)

(b)

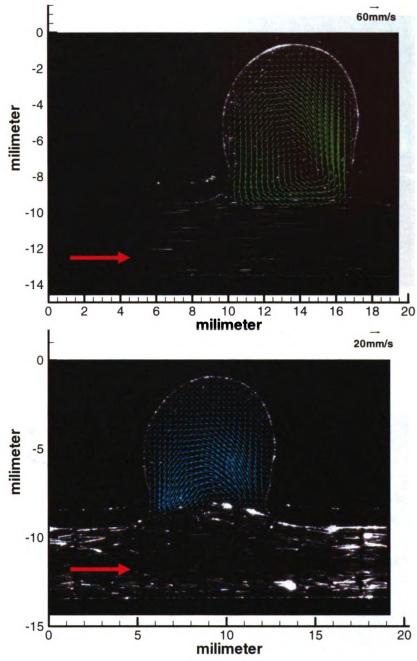

Figure 2. Comparison of velocity field within the aneurysm (a) without stent (b) with stent at a Reynolds number of 184. The arrow shows the flow direction in the tube. Inside the aneurysm cavity the flow is in counter-clockwise direction.

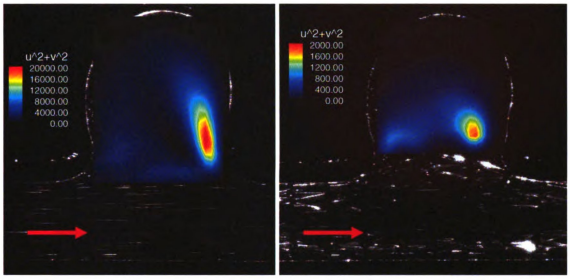

Figure 3. Comparison of total kinetic energy within the aneurysm (a) without stent (b) with stent at a Reynolds number of 184

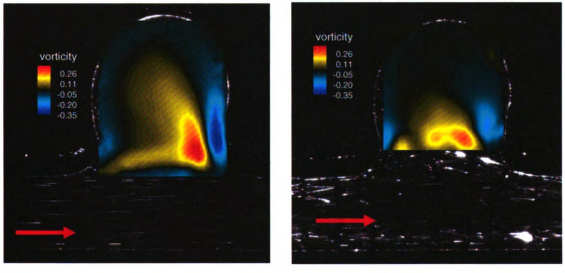

Figure 4. Comparison of vorticity within the aneurysm (a) without stent (b) with stent at a Reynolds number of 184

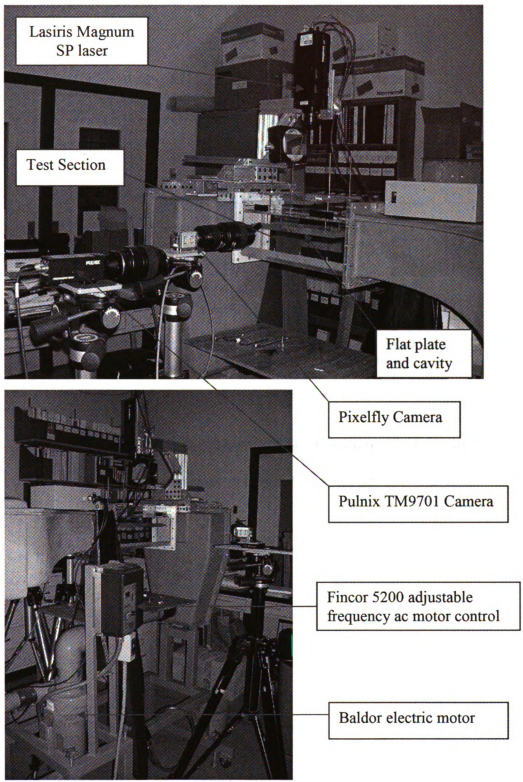

Figure 5. Experimental Set up (a) Rear View (b) Front view

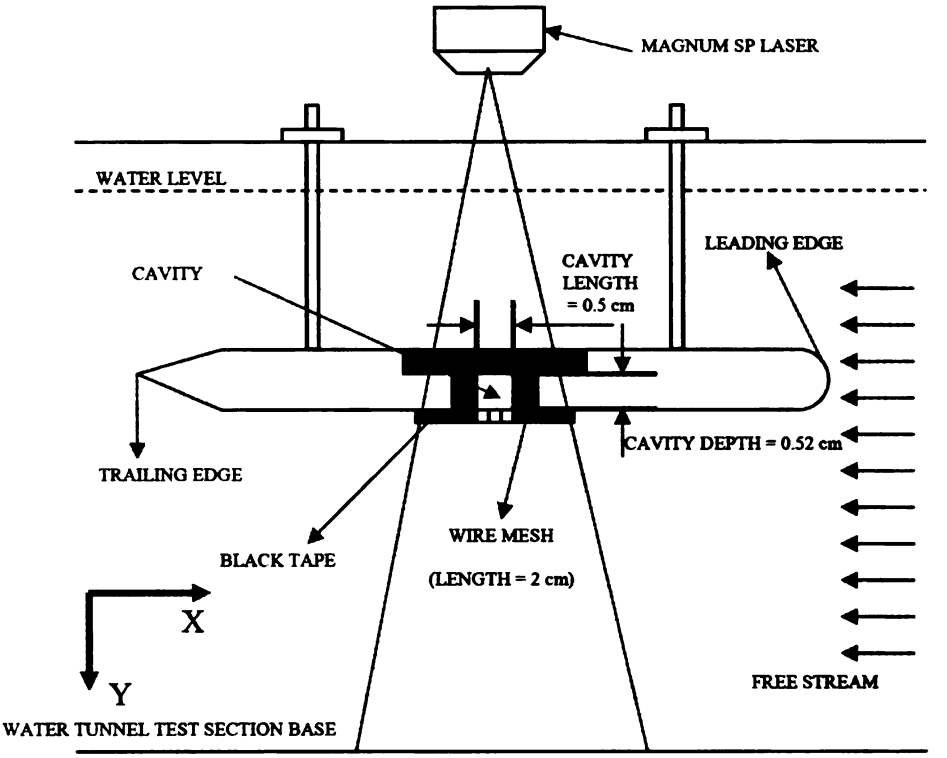

Figure 6. Schematic of flat plate with the cavity. The dimensions of cavity are 0.5 cm (length) x 0.52 cm (depth). The dimensions in the schematic are not shown to scale.

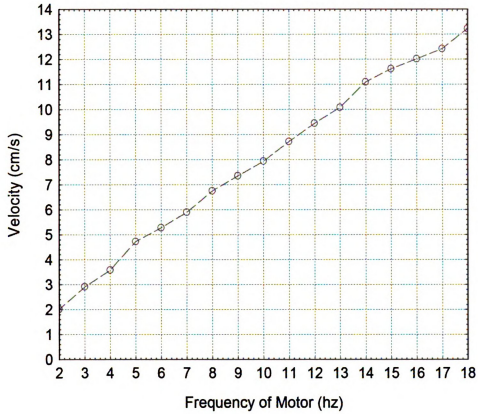

Figure 7. Water Tunnel Calibration

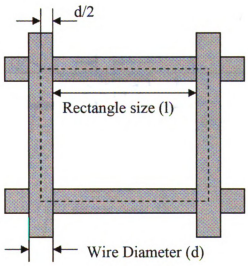

Figure 8. Definition of rectangle size.

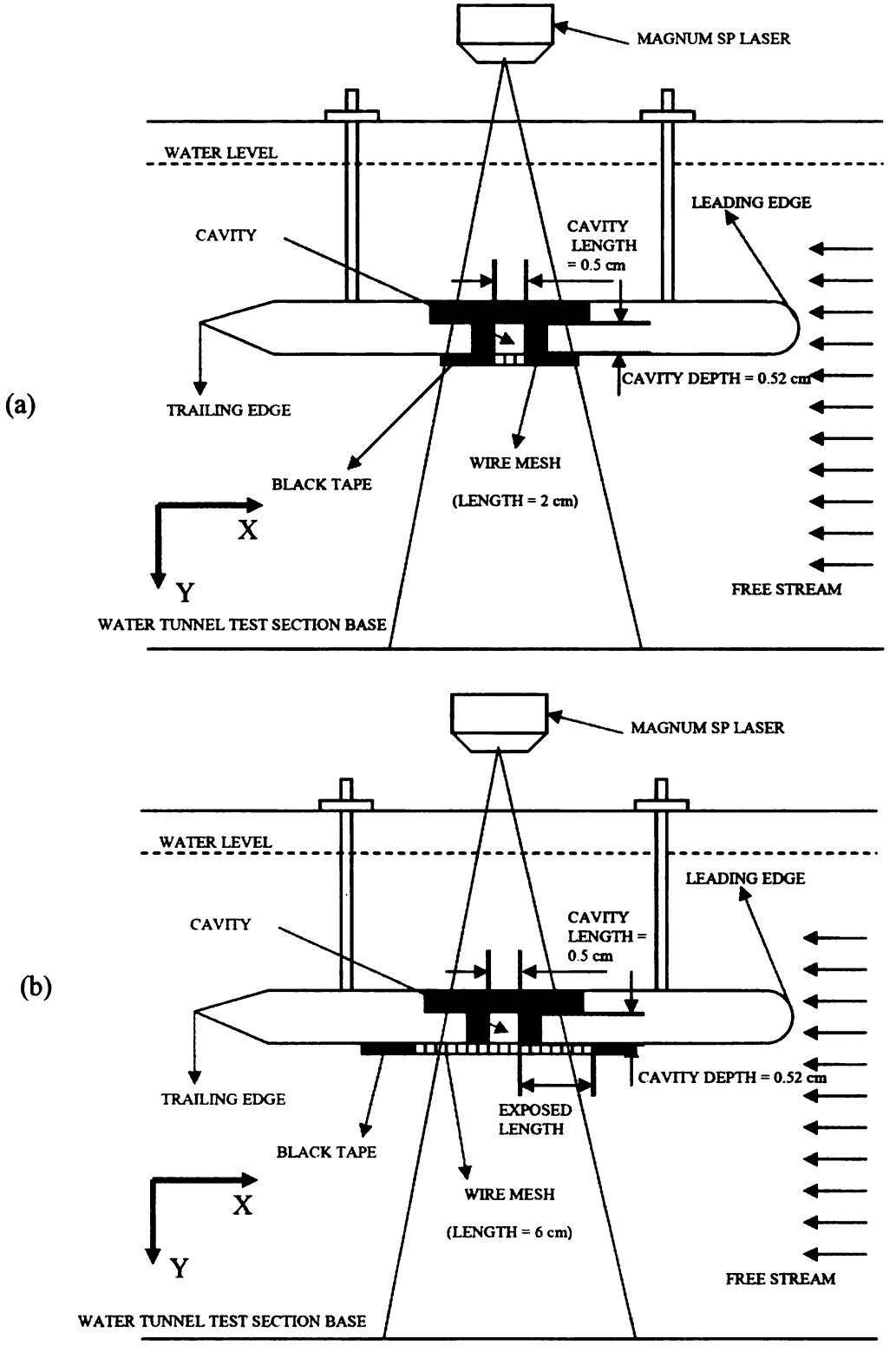

Figure 9. Schematic of test section for the experiment (a) Effect of percentage opening area/ rectangle size (b) Effect of exposed length of mesh

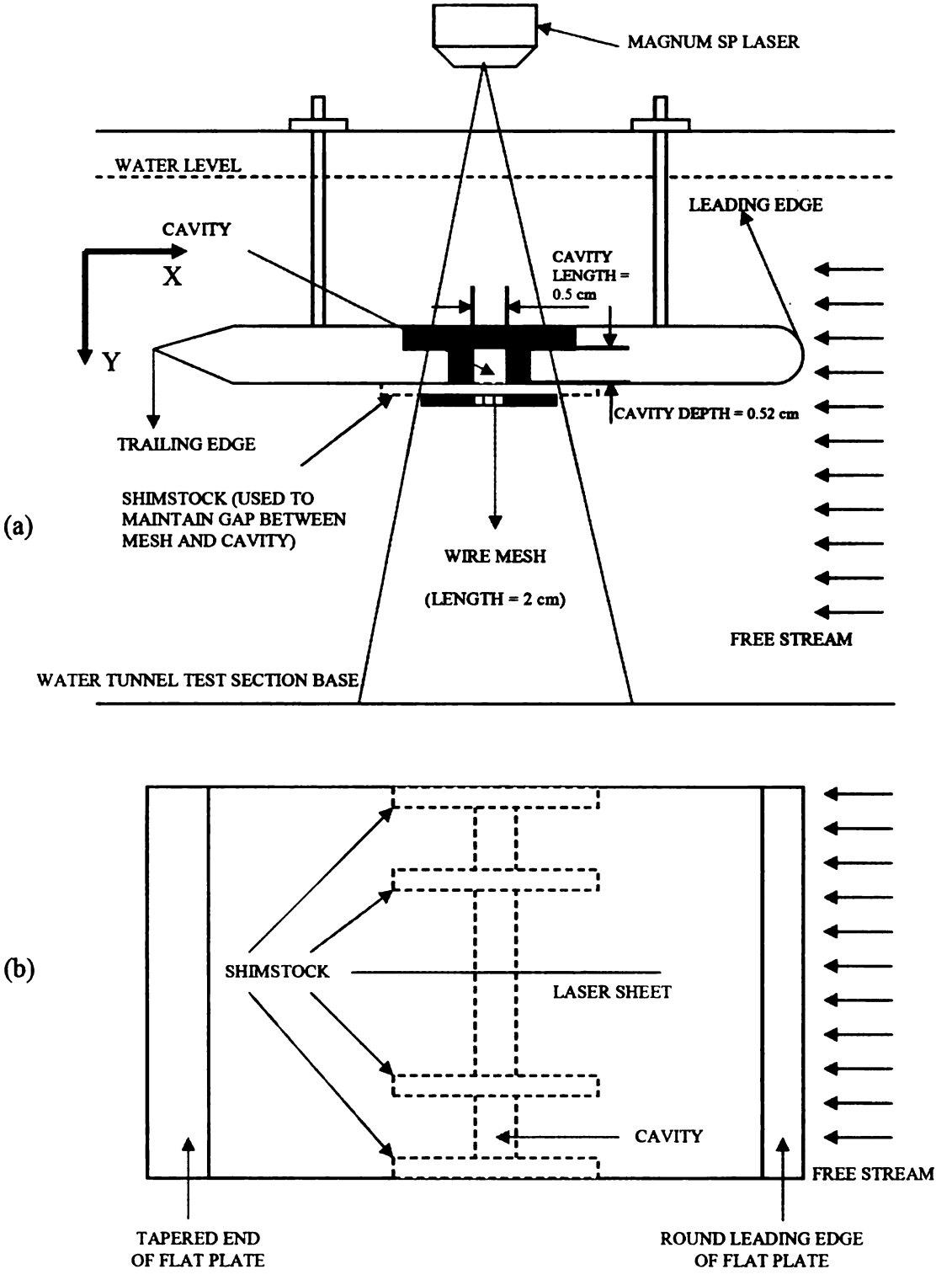

Figure 10. Schematic of test section for the experiment - effect of gap between the mesh and the cavity (a) Front view (b) Top view of flat plate

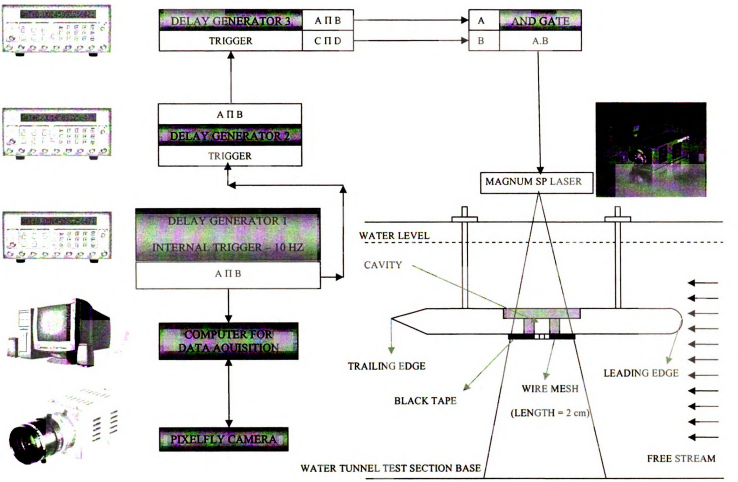

Figure 11. Streamwise imaging arrangement for Pixelfly camera

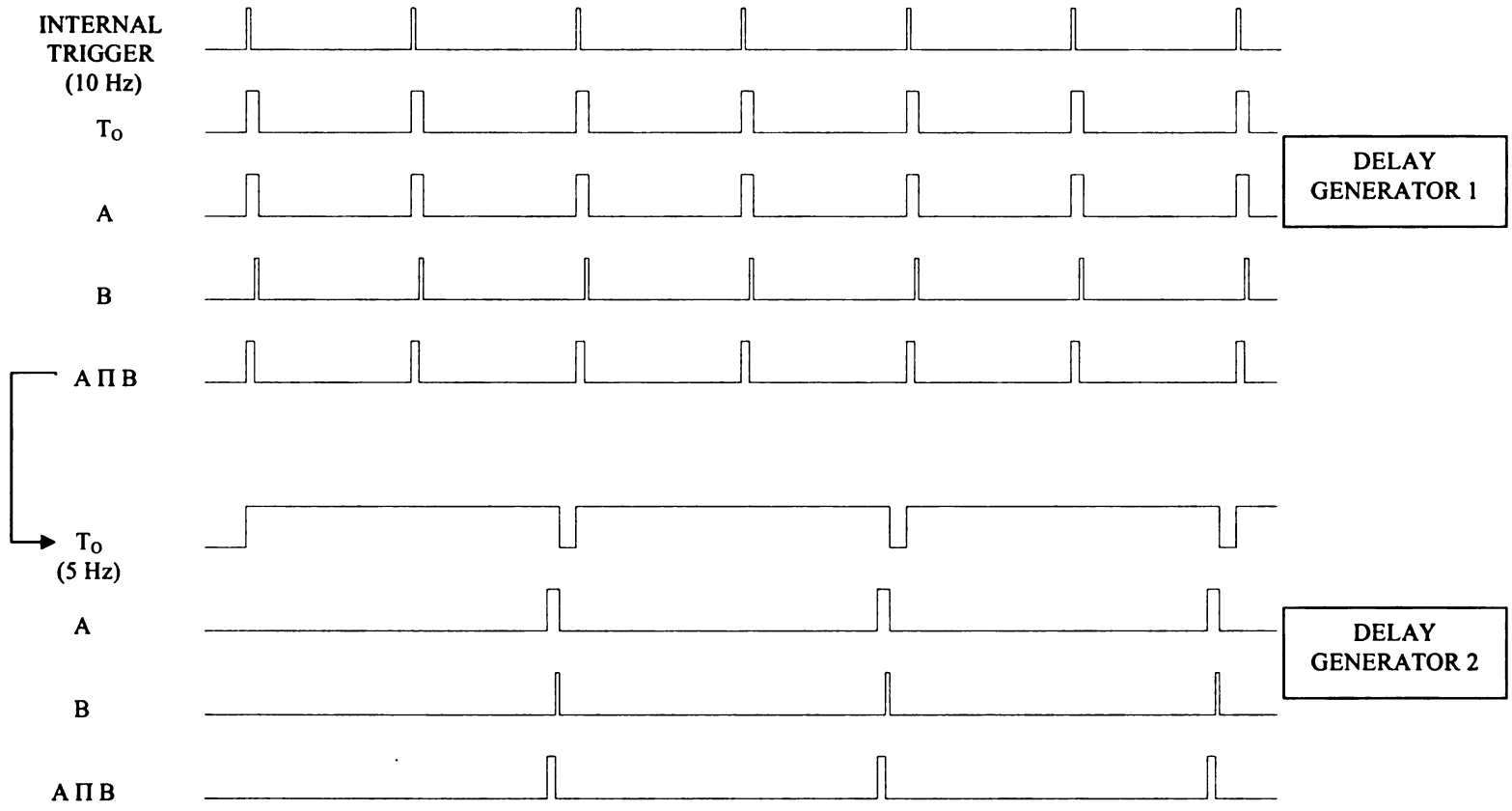

Figure 12. Schematic of timing diagram for Pixelfly camera. In this figure timing diagram is shown only for two delay generators. The remaining timing diagram is shown in the next page.

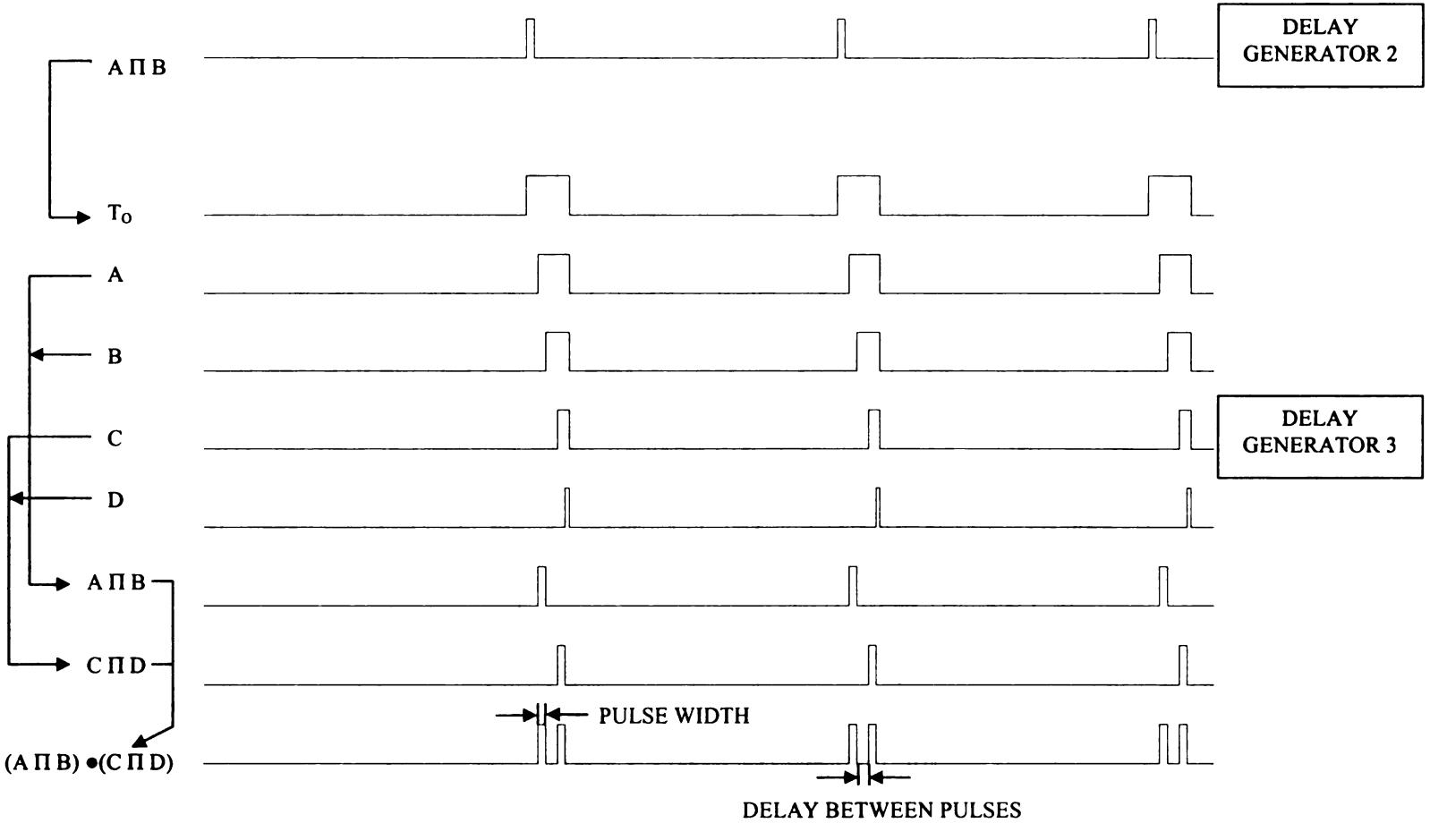

Figure 13. Continuation of schematic of timing diagram for Pixelfly camera.

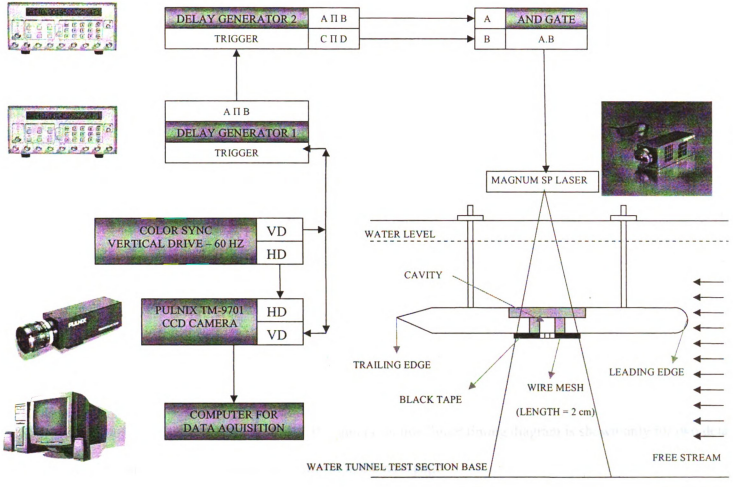

Figure 14. Streamwise imaging arrangement for Pulnix TM – 9701 CCD camera

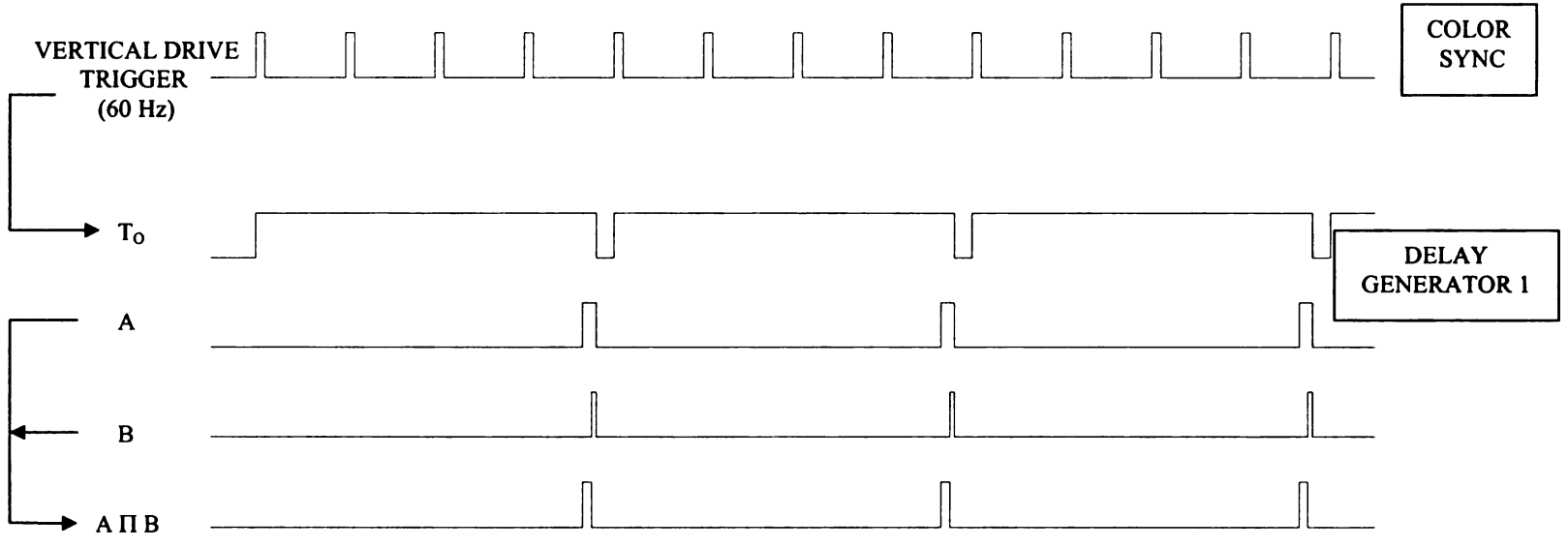

Figure 15. Schematic of timing diagram for Pulnix TM-9701 camera. In this figure timing diagram is shown only for two delay generators. The remaining timing diagram is shown in the next page.

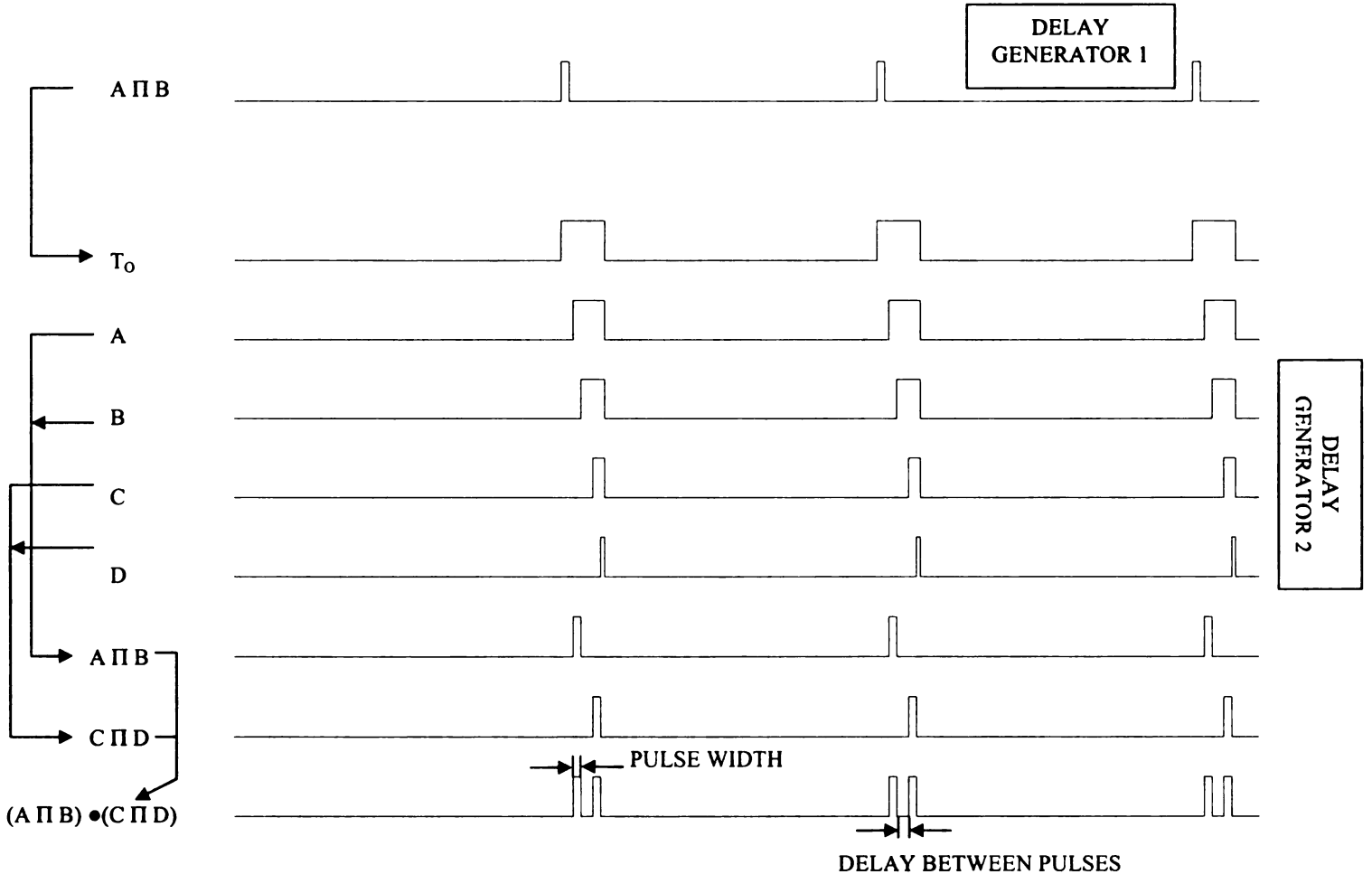

Figure 16. Continuation of schematic of timing diagram for Pulnix TM-9701 camera.

(a)

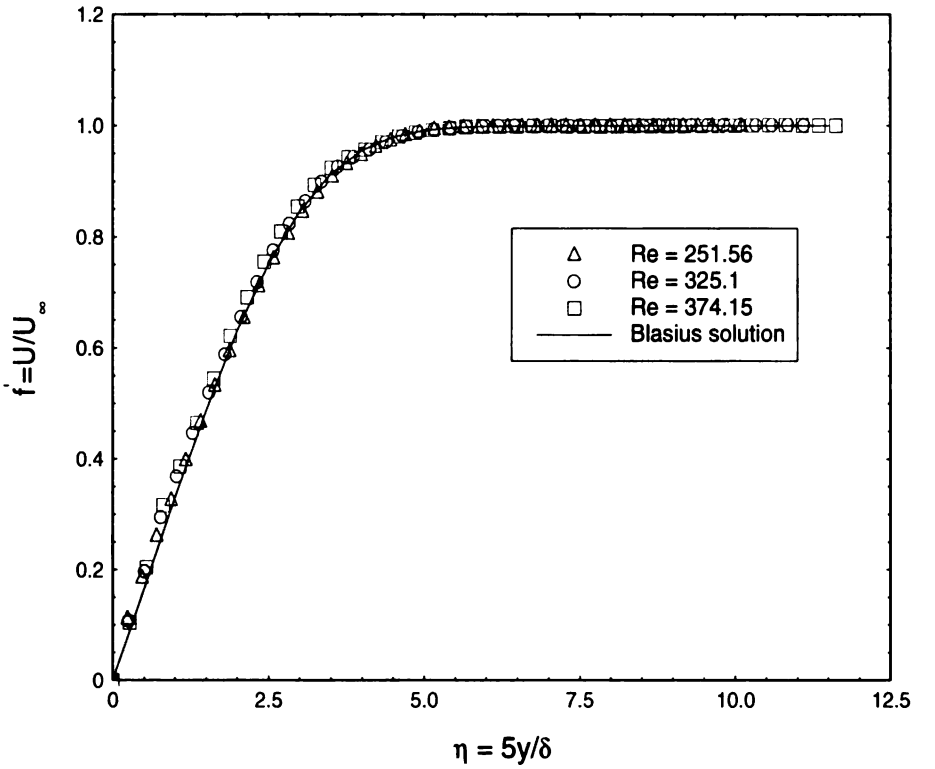

(b)

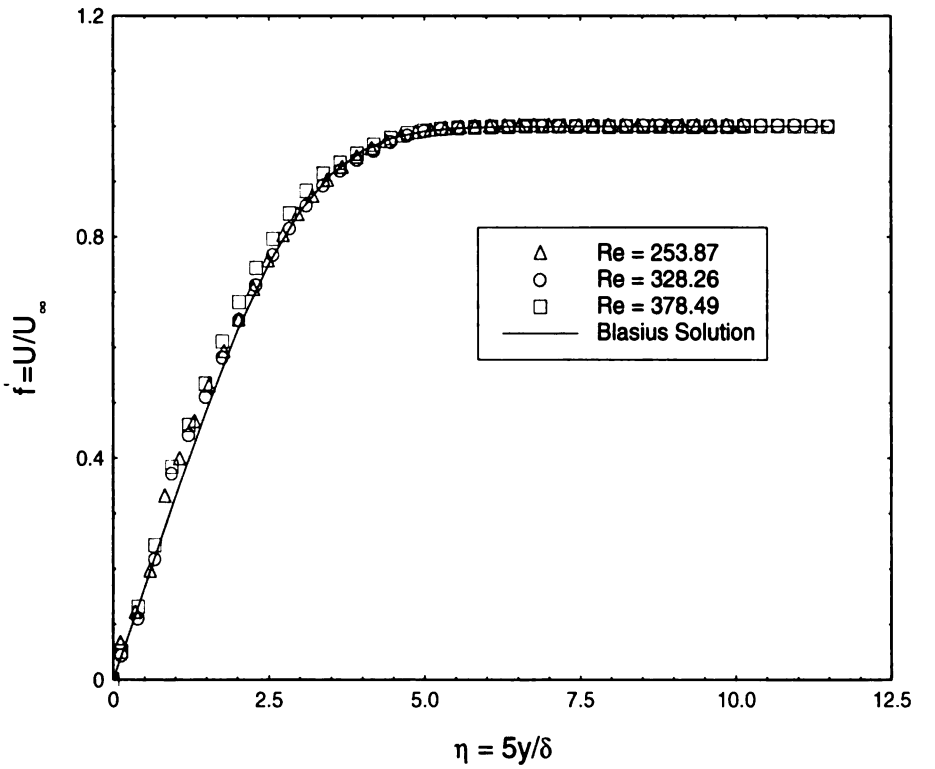

Figure 17. Comparison of measured velocity profiles with Blasius solution at a section,

(a) 1.8cm (b) 0.04cm upstream of the front edge of the cavity

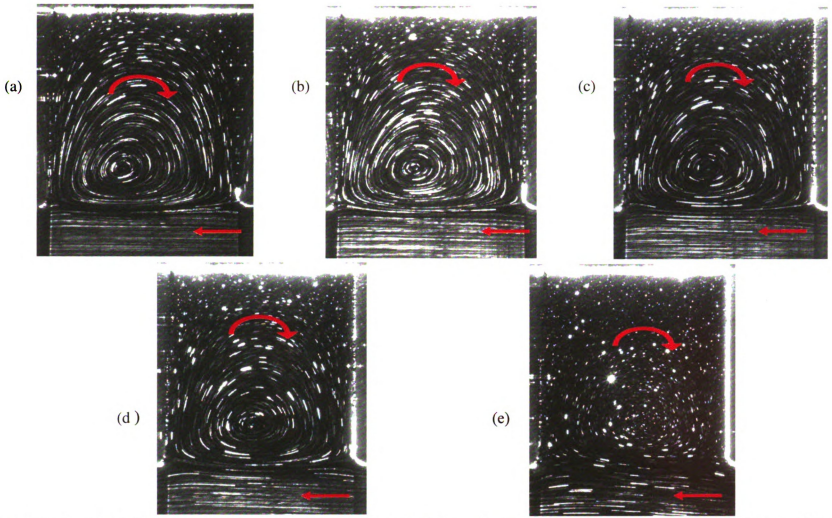

Figure 18. Flow visualization inside the cavity for no mesh case at Reynolds number (a) 390 (b) 325 (c) 255 (d) 179 (e) 100. The arrows show the flow direction. The flow circulates in the clockwise direction inside the cavity.

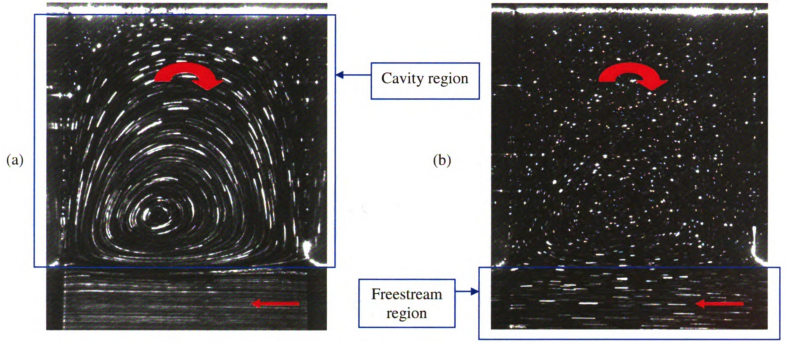

Figure 19. Comparison of flow field between the cavity and free stream, for no mesh case at a Reynolds Number of 390. The exposure times are (a) 400 ms (b) 20ms. The flow circulates in the clockwise direction inside the cavity.

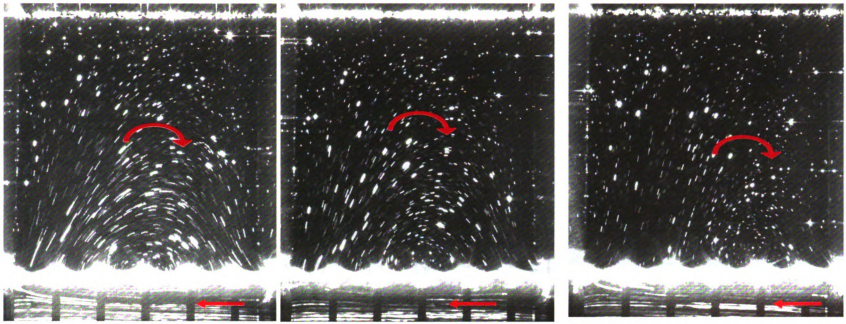

(a) (b) (c)

Figure 20. Flow visualization inside the cavity, which is covered with the mesh of 0.1905 mm diameter, 64.8% opening area, at Reynolds number (a) 390 (b) 325 (c) 255. The flow circulates in the clockwise direction inside the cavity.

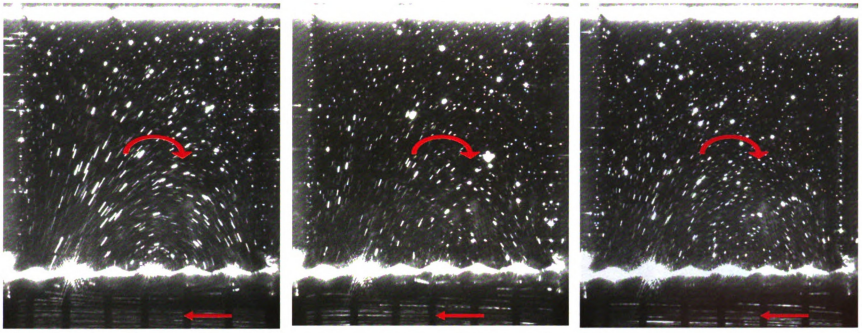

(a) (b) (c)

Figure 21. Flow visualization inside the cavity, which is covered with the mesh 0.1651 mm diameter, 64.8% opening area, at Reynolds number (a) 390 (b) 325 (c) 255. The flow circulates in the clockwise direction inside the cavity.

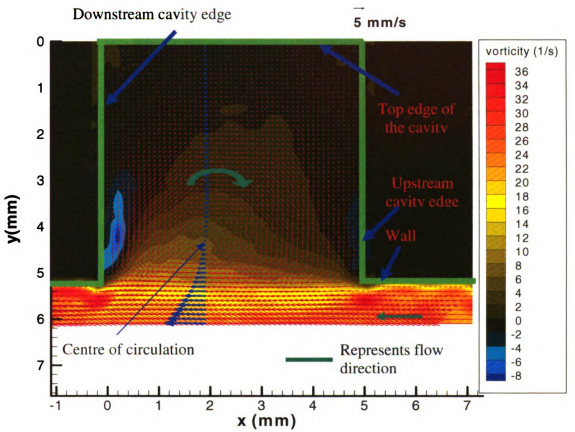

Figure 22. Vorticity distribution (cavity + freestream) for the no mesh case at Reynolds number of 390. The flow circulates in the clockwise direction inside the cavity.

(a)

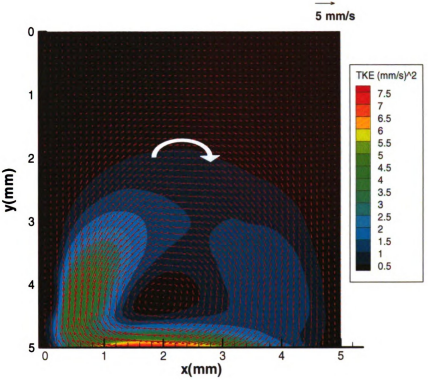

(b)

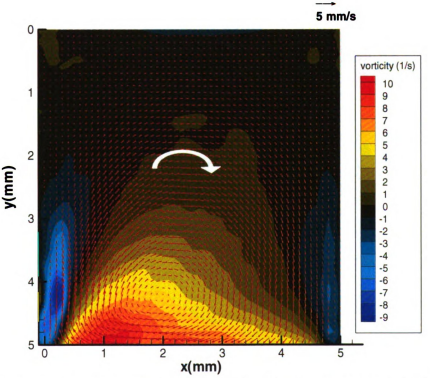

Figure 23. (a) Total kinetic energy distribution (b) Vorticity distribution inside the cavity for the no mesh case at Reynolds number of 390.

(a)

(b)

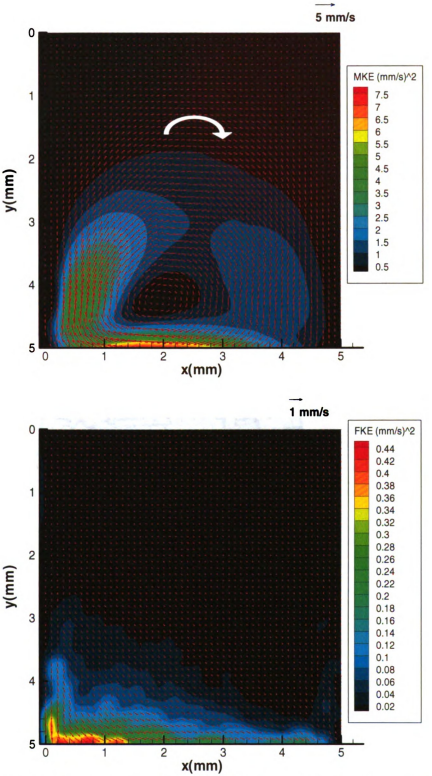

Figure 24. (a) Mean kinetic energy distribution (b) Fluctuating kinetic energy distribution inside the cavity for the no mesh case at Reynolds number of 390.

(a)

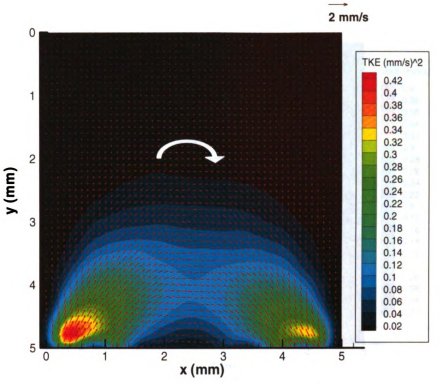

(b)

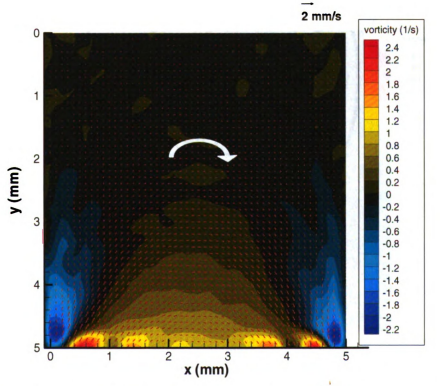

Figure 25. (a) Total kinetic energy distribution (b) Vorticity distribution inside the cavity for the 0.1905 mm diameter, 64.8% opening area mesh at Re of 390.

(a)

(b)

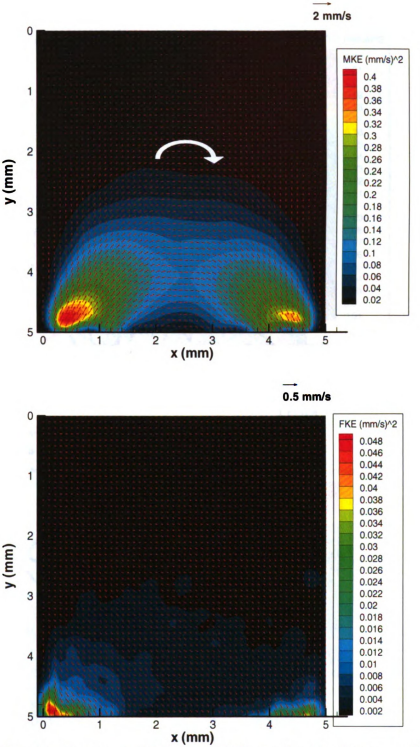

Figure 26. (a) Mean kinetic energy distribution (b) Fluctuating kinetic energy distribution inside the cavity for the 0.1905 mm diameter, 64.8% opening area mesh at Re of 390.

(a)

(b)

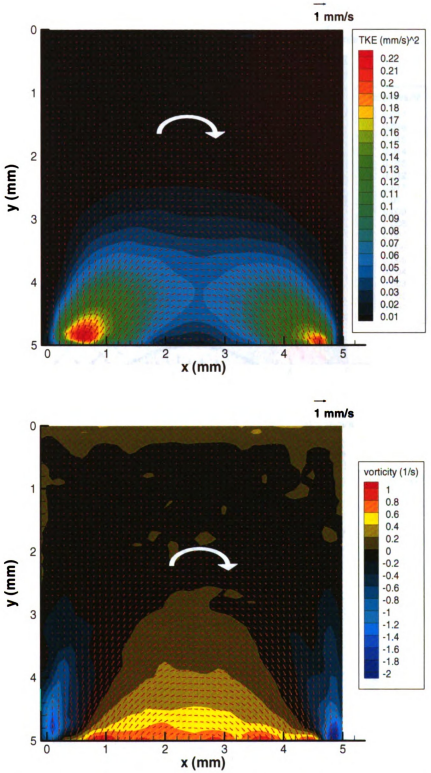

Figure 27. (a) Total kinetic energy distribution (b) Vorticity distribution inside the cavity for the 0.1651 mm diameter, 64.8% opening area mesh at Re of 390.

(a)

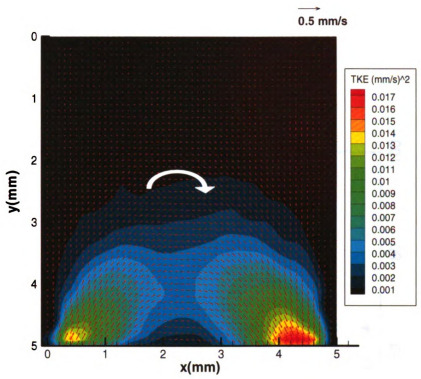

(b)

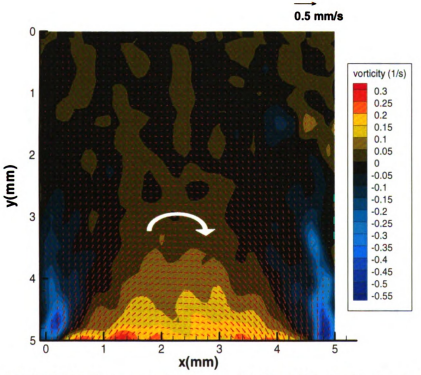

Figure 28. (a) Total kinetic energy distribution (b) Vorticity distribution inside the cavity for the 0.1905 mm diameter, 39.1% opening area mesh at Re of 390.

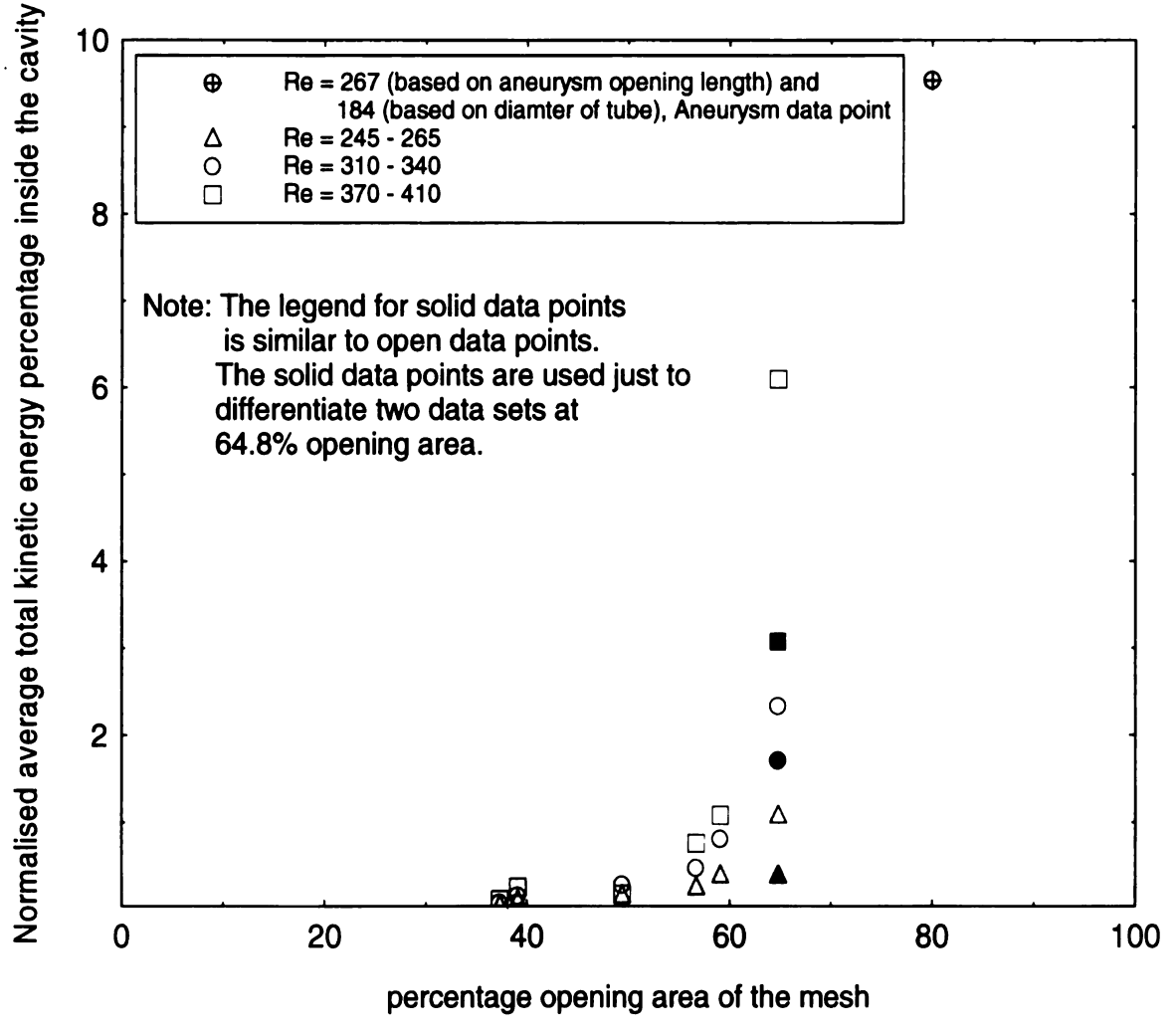

Figure 29. Result for effect of percentage opening area of mesh on normalized average total kinetic energy inside the cavity

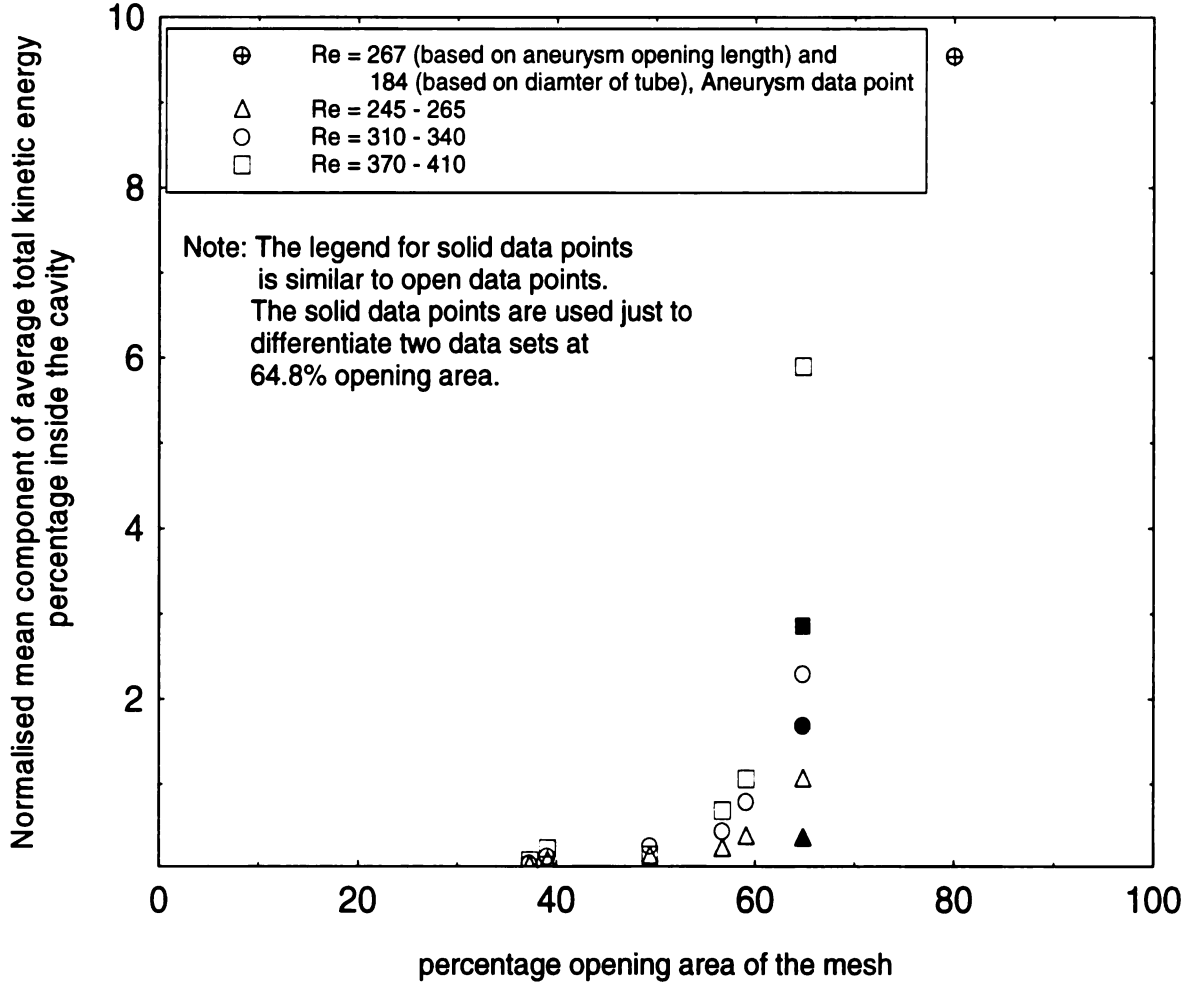

Figure 30. Result for effect of percentage opening area of mesh on normalized mean component of space averaged total kinetic energy inside the cavity

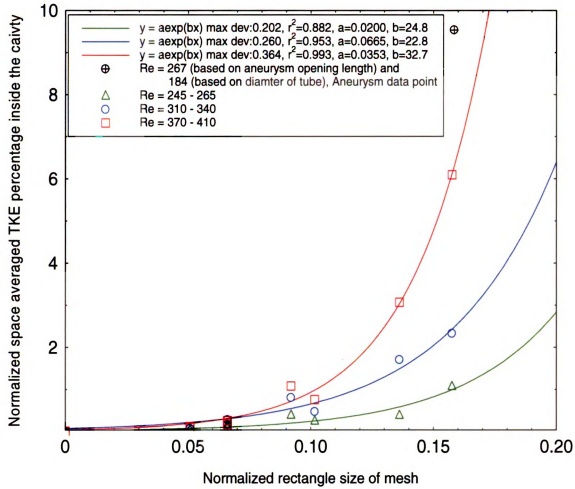

Figure 31. Result for effect of normalized rectangle size of mesh on normalized space averaged total kinetic energy inside the cavity

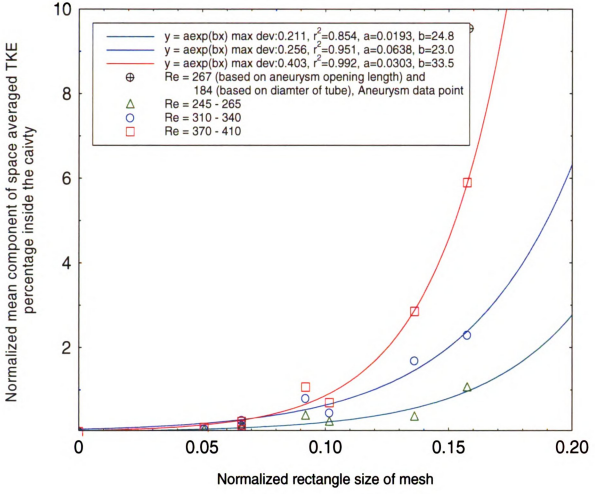

Figure 32. Result for effect of normalized rectangle size of mesh on normalized mean component of space averaged total kinetic energy inside the cavity

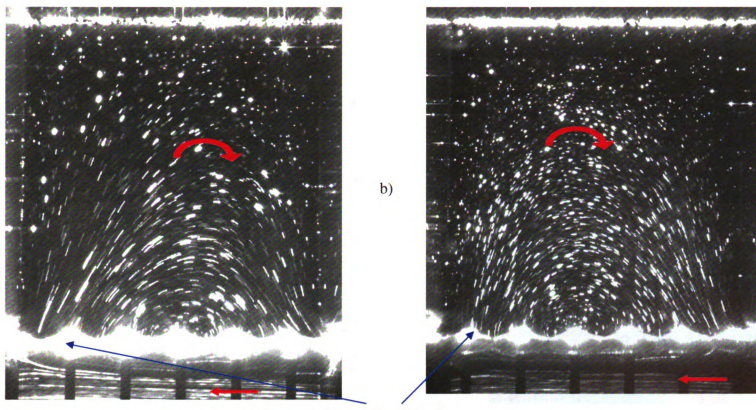

Figure 33. Study of effect of positioning of mesh through particle streak flow visualization inside the cavity, which is covered with the mesh of 0.1905 mm diameter, 64.8% opening area, at Reynolds number 390. The flow circulates in the clockwise direction inside the cavity. First wire of mesh is closer to downstream edge in case (a) compared to case (b)

(a)

(b)

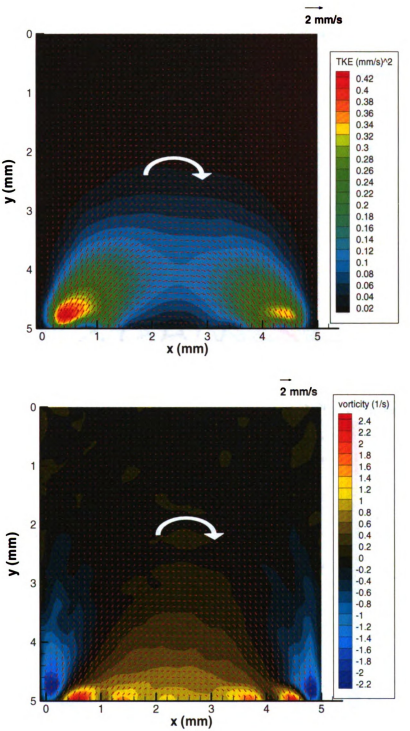

Figure 34. (a) TKE distribution (b) Vorticity distribution inside the cavity for the mesh (0.1905 mm diameter, 64.8% opening area) at Re of 390 whose first wire is at a distance of 0.8 mm from the downstream edge of the cavity.

(a)

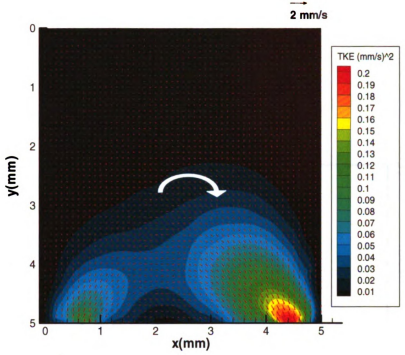

(b)

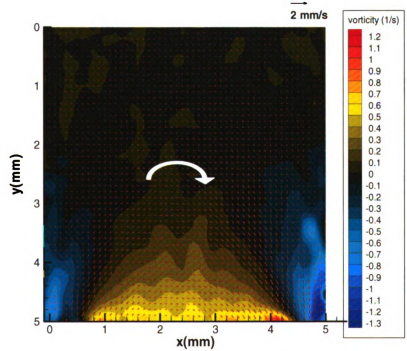

Figure 35. (a) TKE distribution (b) Vorticity distribution inside the cavity for the mesh (0.1905 mm diameter, 64.8% opening area) at Re of 390 whose first wire is at a distance of 0.2 mm from the downstream edge of the cavity.

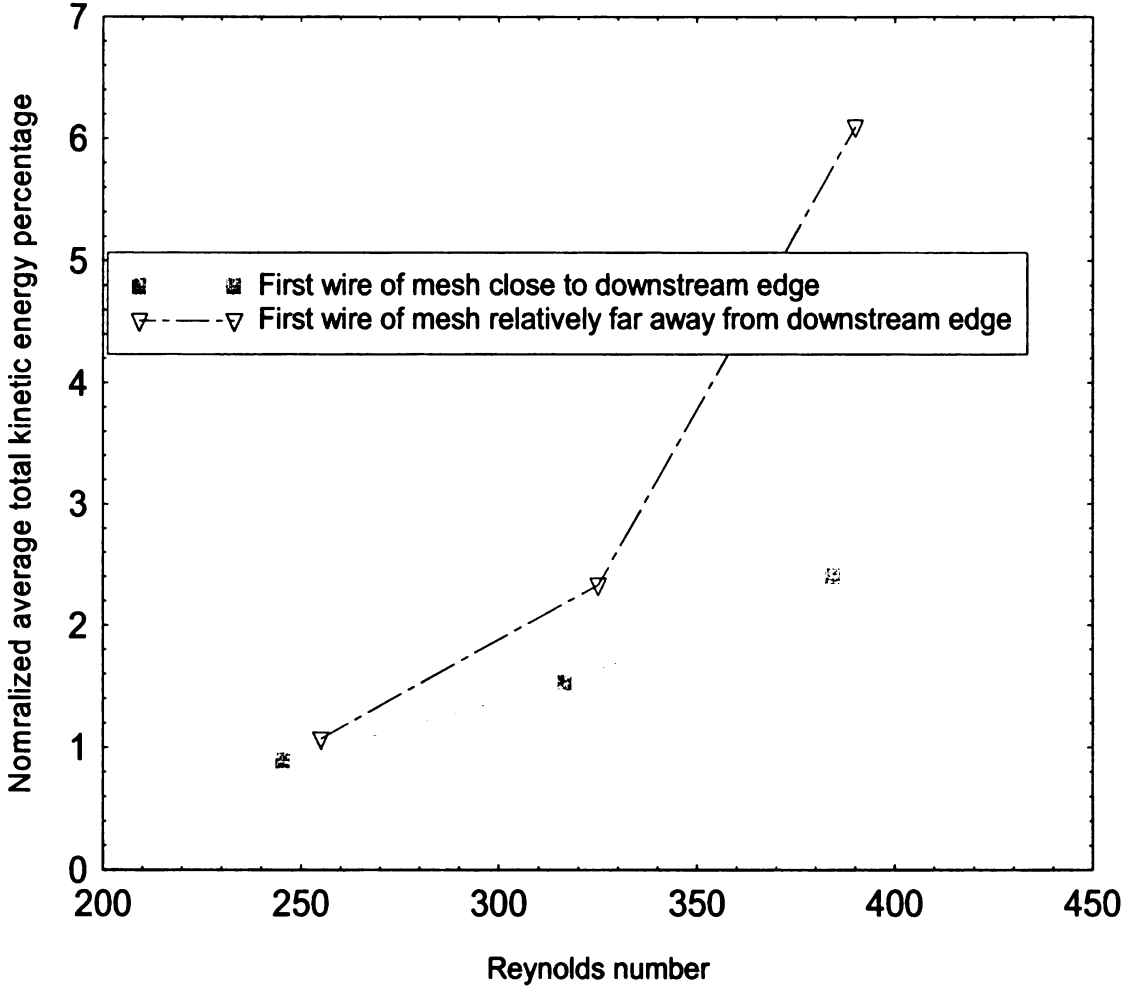

Figure 36. Result for effect of position of mesh with respect to cavity, on normalized space averaged TKE inside the cavity

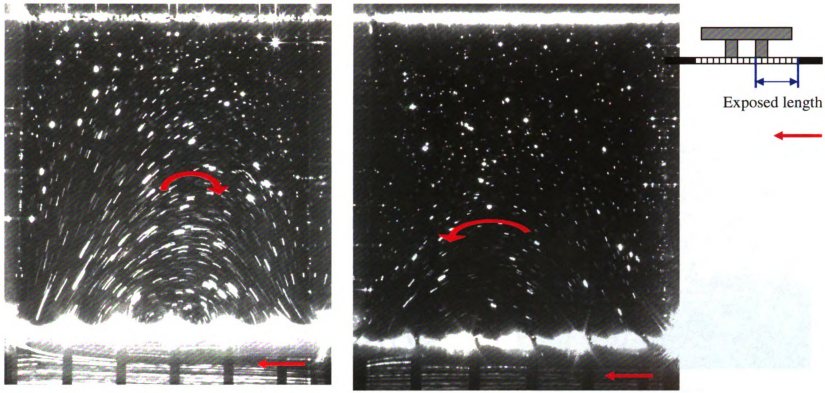

(a) (b)

Figure 37. Study of effect of exposed length of mesh through particle streak flow visualization inside the cavity, which is covered with the mesh of 0.1905 mm diameter, 64.8% opening area, at Reynolds number ≈ 390. Exposed length of mesh is (a) 0 cm (b) 2 cm. The flow circulates in the (a) clockwise direction (b) anticlockwise direction inside the cavity.

(a)

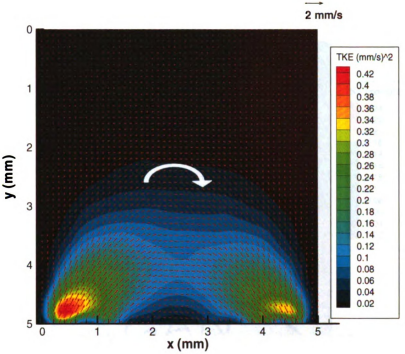

(b)

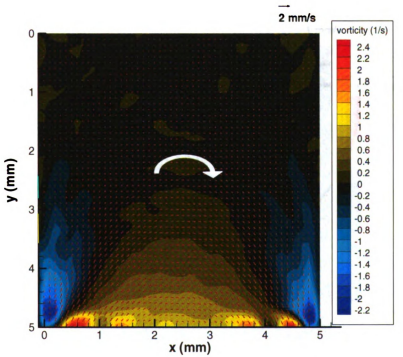

Figure 38. (a) TKE distribution (b) Vorticity distribution inside the cavity for 0 cm exposed length of mesh (0.1905 mm diameter, 64.8% opening area) at Re of 390.

(a)

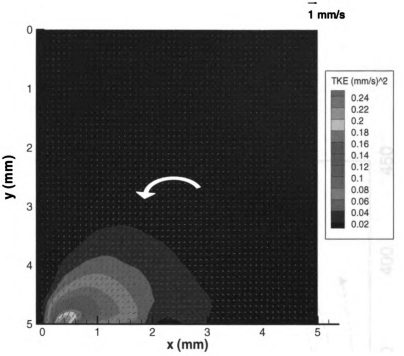

(b)

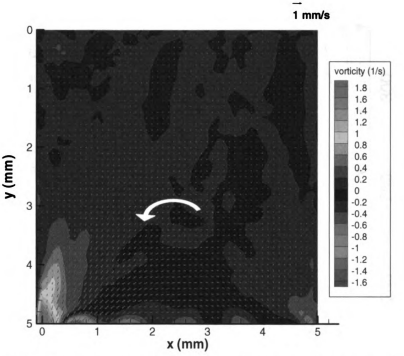

Figure 39. (a) TKE distribution (b) Vorticity distribution inside the cavity for a 2 cm exposed length of mesh (0.1905 mm diameter, 64.8% opening area) at Re ≈ 390.

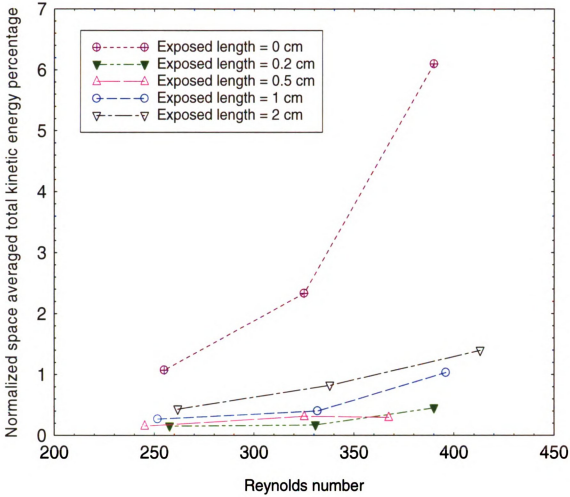

Figure 40. Result for effect of exposed length mesh on normalized space averaged total kinetic energy inside the cavity

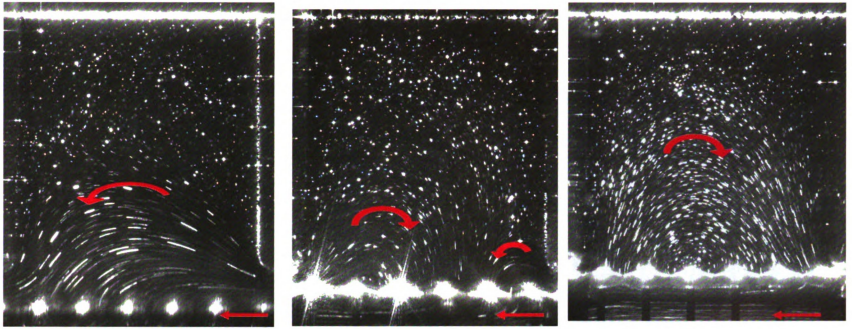

(a) (b) (c)

Figure 41. Study of effect of gap between the mesh and the cavity, through particle streak flow visualization inside the cavity, which is covered with the mesh of 0.1905 mm diameter, 64.8% opening area, at Reynolds number ≈ 390. Gap is (a) 0.508 mm (b) 0.127 mm (c) 0 mm. The flow circulates in the (a) anticlockwise direction (b) clockwise near downstream edge and anticlockwise near upstream edge (c) clockwise direction inside the cavity.

(a)

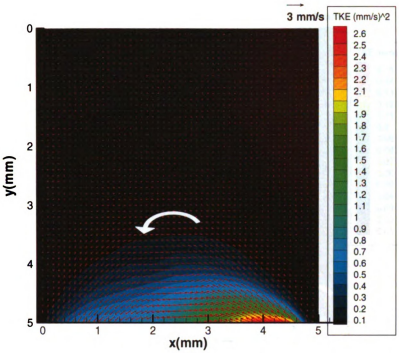

(b)

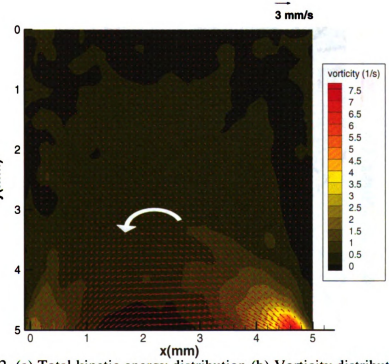

Figure 42. (a) Total kinetic energy distribution (b) Vorticity distribution inside the cavity for a gap of 0.508 mm between the mesh (0.1905 mm diameter, 64.8% opening area) and the cavity at Reynolds number of 392.7.

(a)

(b)

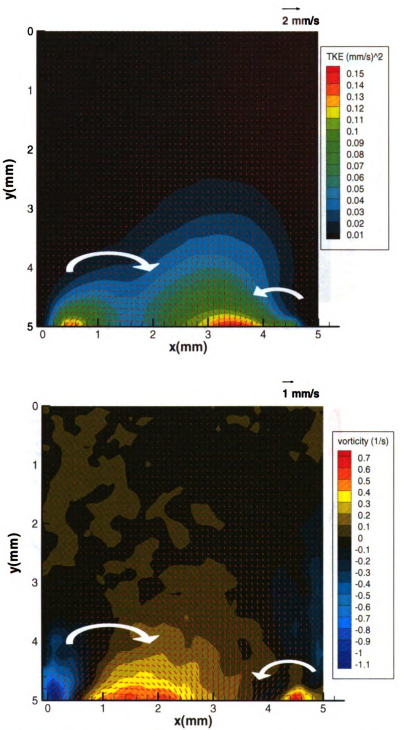

Figure 43. (a) Total kinetic energy distribution (b) Vorticity distribution inside the cavity for a gap of 0.127 mm between the mesh (0.1905 mm diameter, 64.8% opening area) and the cavity at Reynolds number of 406.

(a)

(b)

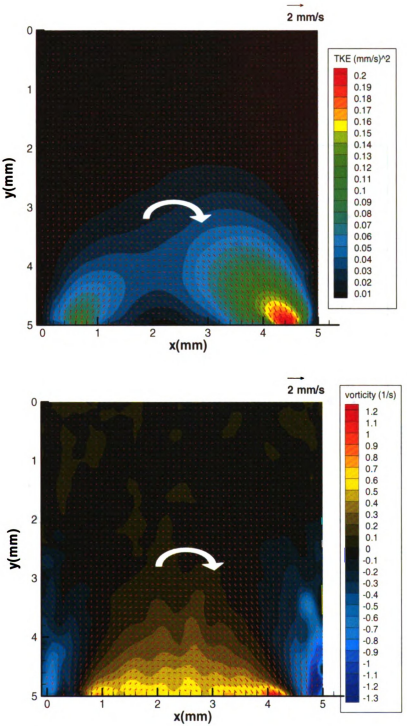

Figure 44. (a) Total kinetic energy distribution (b) Vorticity distribution inside the cavity for a gap of 0 mm between the mesh (0.1905 mm diameter, 64.8% opening area) and the cavity at Reynolds number of 406.

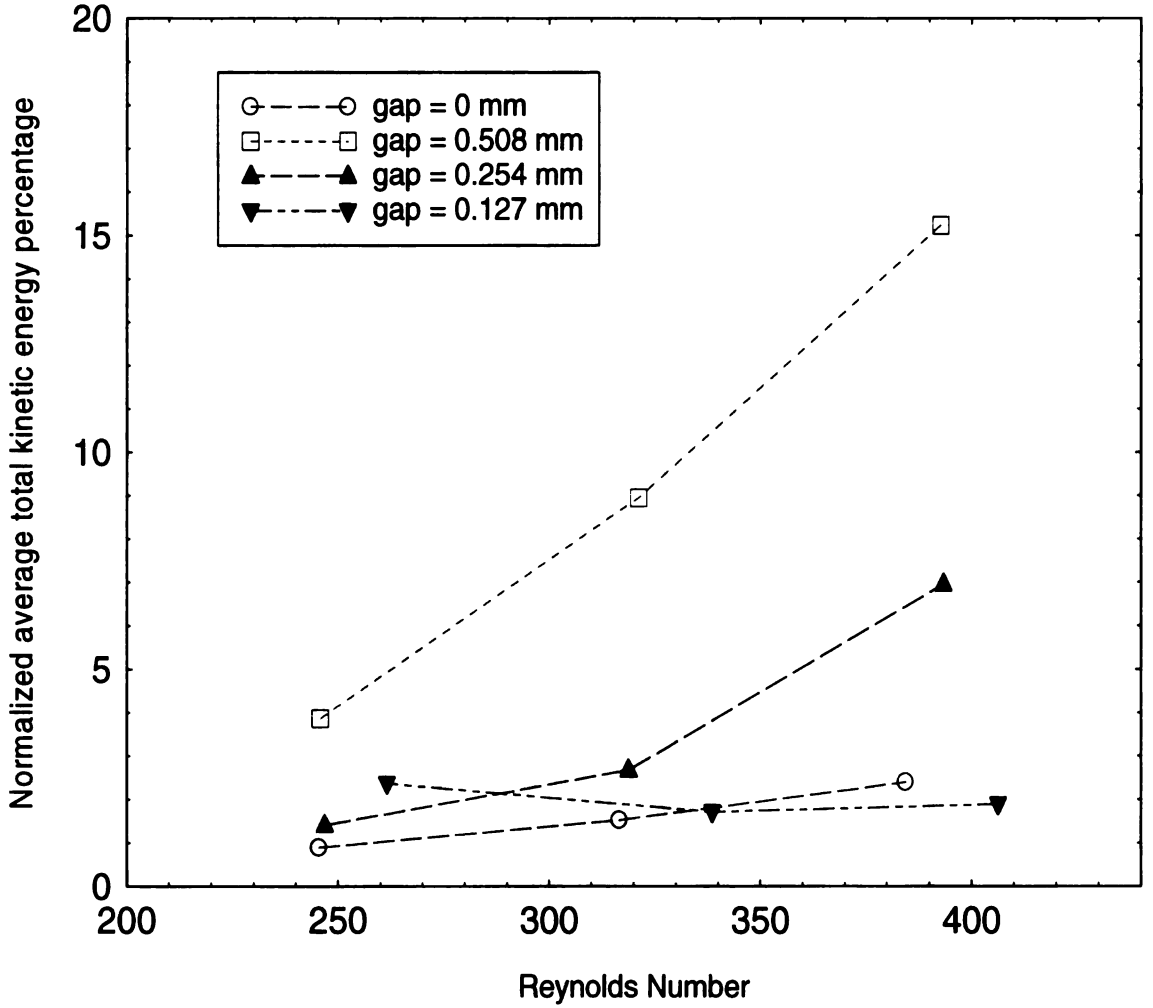

Figure 45. Result for effect of gap between mesh and the cavity on normalized space averaged total kinetic energy inside the cavity

LIST OF REFERENCES

Aydin, M. and Fenner, R. T. (2001), "Boundary element analysis of driven cavity flow for low and moderate Reynolds number," International Journal for Numerical Methods in Fluids, Vol. 37, pp. 45-64

Chee Lum (2007), "Experimental investigation of flow field inside a glass model of a brain aneurysm"

Chiang, T.P., Sheu, W.H. and Robert R. Hwang (1998), "Effect of Reynolds number on the eddy structure in a lid-driven cavity," International Journal for Numerical Methods in Fluids, Vol. 26, pp. 557-579.

Eames, I. and Gilbertson, M.A. (2004), "The settling and dispersion of smell dense particles by spherical vortices," Journal of Fluid Mechanics, Vol. 498, pp 183-203.

Kawaguti, M. (1961), "Numerical Solution of the Navier-Stokes equations for a flow in a two-dimensional cavity," Journal of the Physical Society of Japan, Vol. 16, pp. 2307-2315.

Kinoshita, O. and Ito, H. (1984), "Experimental analysis of two-dimensional cavity flow at very low Reynolds numbers," Journal of Fluid Control (ISSN 0015-4687), vol. 15, pp. 65-77.

Lieber, B.B., Stancampiano, A.P. and Wakhlooo, A.K. (1997), "Alteration of hemodynamics in aneurysm models by stenting: Influence of stent porosity," Annals of Biomedical Engineering, Vol. 25, pp. 460-469.

Manovski, P. (2005) "Experimental characterization of low Reynolds number flow past a cavity," Graduate yearbook 2005, Department of Mechanical Engineering, Monash University

Moffatt, H.K. (1964), "Viscous and resistive eddies near a sharp corner," Journal of Fluid Mechanics, Vol. 18, pp. 1-18.

Power, H. and Botte, V. (1998), "An indirect boundary element method for low Reynolds number Navier–Stokes equations in a three-dimensional cavity," International Journal for Numerical Methods in Engineering, Vol.41, pp. 1485–1505.

Rhee, K., Han, M.H. and Cha S.H. (2002), "Changes of Flow Characteristics by stenting in aneurysm models: Influence of Aneurysm geometry and stent porosity," Annals of Biomedical Engineering, Vol. 30, pp. 894-904.

Takematsu, M. (1966), "Slow viscous flow past a cavity," Journal of the Physical Society of Japan, Vol. 18, pp. 1816-1821.

Yu, S.C.M., Zhao, J.B. (1999), "A steady flow analysis on the stented and non-stented sidewall aneurysm models," Medical Engineering & Physics, Vol. 21, pp. 133-141.

Zhou1, Y.C., Patnaik, B.S.V., Wan, B.C. and Wei1 G.W. (2003), "DSC solution for flow in a staggered double lid driven cavity," International Journal for Numerical Methods in Engineering, Vol. 57, pp. 211-234.


MICHIGAN STATE UNIVERSITY L
3 1293 02956 2